



6G BRAINS Deliverable D3.3

Multiband characterization of propagation in industry scenarios

Editor:	Xun ZHANG (ISEP)
Deliverable nature:	Report (R)
Dissemination level: (Confidentiality)	Public (PU)
Contractual delivery date:	April 2023 (M28)
Actual delivery date:	09 November 2023
Suggested readers:	Consortium members, reviewers, researchers, designers of networks in industry environments
Version:	1.0
Total number of pages:	44
Keywords:	OWC, multiband propagation, multiband channel modelling

Abstract

The present report introduces the measurement results and parameter estimation for multi-band channel modelling in Industry scenario. The measurements were conducted in a Bosch factory and in a laboratory at Fraunhofer facilities, both in Germany. After the measurements, the data needed to be analysed and prepared for the calibration of the channel modelling task presented in Deliverable D3.4. This deliverable presents validation research to enable new cross-frequency services for the industry environment but in the same way, these results are essential for development of new cross-frequency services in other areas such as V2V or Smart Home. The understanding of the different physical propagation properties of the frequency bands from Sub-6 GHz to THz and OWC enables the creation of a unique framework for further developments in 6G, which is currently unique in the world.

Disclaimer

This document contains material, which is the copyright of certain 6G BRAINS consortium parties, and may not be reproduced or copied without permission.

In case of Public (PU):

All 6G BRAINS consortium parties have agreed to full publication of this document.

In case of Restricted to Programme (PP):

All 6G BRAINS consortium parties have agreed to make this document available on request to other framework programme participants.

In case of Restricted to Group (RE):

All 6G BRAINS consortium parties have agreed to full publication of this document. However this document is written for being used by <organisation / other project / company etc.> as <a contribution to standardisation / material for consideration in product development etc.>.

In case of Consortium confidential (CO):

The information contained in this document is the proprietary confidential information of the 6G BRAINS consortium and may not be disclosed except in accordance with the consortium agreement.

The commercial use of any information contained in this document may require a license from the proprietor of that information.

Neither the 6G BRAINS consortium as a whole, nor a certain part of the 6G BRAINS consortium warrant that the information contained in this document is capable of use, nor that use of the information is free from risk, accepting no liability for loss or damage suffered by any person using this information.

The EC flag in this document is owned by the European Commission and the 5G PPP logo is owned by the 5G PPP initiative. The use of the EC flag and the 5G PPP logo reflects that 6G BRAINS receives funding from the European Commission, integrated in its 5G PPP initiative. Apart from this, the European Commission and the 5G PPP initiative have no responsibility for the content of this document.

The research leading to these results has received funding from the European Union Horizon 2020 Programme under grant agreement number 101017226 – 6G BRAINS – H2020-ICT-2020-2.

Impressum

[Full project title]	Bring Reinforcement-learning Into Radio Light Network for Massive Connections
[Short project title]	6G BRAINS
[Number and title of work-package]	WP3: 6G Physical Propagation Measurements and Modelling, from Microwave to THz and OWC
[Number and title of task]	T3.1: Multi-Band (MW + mmWave + THz + OWC) Channel Measurements in the Industrial Network Environments and Industrial Applications T3.2: Analysis of measurement data and elaboration of the differences in wave propagation T3.3: Common fused channel model for the industrial network environments and industrial
[Document title]	Multiband characterization of propagation in industry scenarios
[Editor: Name, company]	Xun ZHANG, ISEP
[Work-package leader: Name, company]	Diego DUPLEICH, FhG
[Estimation of PM spent on the Deliverable]	20

Executive summary

This document is a deliverable from the 6G BRAINS project, which focuses on developing wireless communication-enabled industrial manufacturing. Full spectrum communication, including sub-6 GHz, mmWave, THz, and optical band-enabled communication, is emerging as a valuable solution to tackle the challenges of spectrum resource scarcity and the higher key performance indicators (KPIs) required for 6G networks. However, mmWave, THz, optical band signals cannot easily penetrate obstacles, resulting in highly intermittent of these links. This presents a significant challenge for wireless applications in complex industrial environments. Fortunately, obstacles in industrial scenarios typically have fixed positions and directions. Consequently, studying the channel characteristics of these band in industrial settings is crucial for establishing high-reliability communication within the mmWave, THz, optical frequency range.

Therefore, the document provides a detailed report on the measurement results and parameter estimation for channel modelling in multi-band communication. The main contribution of this deliverable is to provide insights into the channel characteristics of multi-band communication in practical and complex environments. Specifically, the sub-6 GHz, mmWave and optical band-based wireless communication channel measurements are performed in large industrial scenario. Moreover, the sub-6 GHz, mmWave and sub-THz band-based wireless communication channel measurements are conducted in machine laboratory.

Based on the practical channel measurement and analysis results, it is important to highlight that non-line-of-sight (NLOS) paths significantly impact channel characteristics in real-world environments. This challenges the notion of channel sparsity in complex settings. Corresponding, strategic transceiver deployment plays a pivotal role in augmenting channel sparsity and elevating overall channel quality. Moreover, it is imperative to reevaluate the proposed channel estimation approach and refine resource allocation and optimization strategies at the physical layer, grounded in an understanding of channel sparsity. These efforts are essential for bolstering the resilience of wireless communication networks in practical industrial settings. Overall, this deliverable first highlights the potential of multi-band communication channel measurement for high-speed information transmission and high-precision positioning services in wireless communication-enabled industrial manufacturing. It also suggests future research directions to further improve the channel modelling and analysis.

List of authors

Company	Author	Contribution
FhG	Diego Dupleich, Alexander Ebert, Yanneck Völker-Schöneberg, Damir Sitdikov, Han Niu	Section I, II, III, IV, and VI
ISEP	Xun Zhang, Xiaodong Liu, Wafa NJMA	Section I, IV, and VI
ULEIC	Huiyu Zhou, Bohan Li, Guoqing Xia	Several sections
BOSCH	Alexander Artemenko, Uwe Wostradowski	Section III and IV: Organization and leading of the OWC channel measurements in Bosch plant
EURES	Anastasius Gavras	Final review

Table of Contents

<i>Executive summary</i>	4
<i>List of authors</i>	5
<i>Table of Contents</i>	6
<i>List of figures and tables</i>	7
<i>Abbreviations</i>	8
1 Introduction	11
2 Scenarios	13
2.1 Machine Room.....	13
2.2 Industry Hall	13
3 Multiband Sub-6 GHz and mmWave Propagation Measurements and Analysis Results in Large Industrial Scenario	15
3.1 Measurement Set-up.....	15
3.2 Temporal Properties of the Propagation Channel	16
3.3 Large-Scale Parameters	17
3.4 Conclusions.....	17
4 OWC Channel measurement and analysis results	18
4.1 OWC front-end description.....	18
4.2 Measurement Set-up.....	19
4.3 Spatial Properties of the Propagation Channel	24
5 Multiband Sub-6 GHz, mmWave, and sub-THz Propagation Measurements and Analysis in Machine Room	29
5.1 Measurement Set-up.....	29
5.2 Spatial Properties of the Propagation Channel	30
5.3 Spatial/Temporal Properties of the Propagation Channel	32
5.4 Temporal Properties of the Propagation Channel	33
5.5 Polarimetric Properties of the Propagation Channel	34
5.6 Analysis of Large-Scale Parameters	36
6 Summary and Concluding Remarks	41
6.1 Summary	41
6.2 Concluding Remarks	42
<i>References</i>	43

List of figures and tables

Figure 1: picture of the machine room scenario taken by the channel sounder (a) TX, and (b) RX.	13
Figure 2: schematic of the industrial hall at BOSCH in Blaichach.....	14
Figure 3: composite picture from the channel sounder (TX) towards the measurement area in the industry hall scenario.....	14
Figure 4: location of the RXs in the industry hall scenario.	16
Figure 5: multi-band isotropic PDP over the different positions in (a) L1 in NLOS and (b) L3 in LOS in the industry hall scenario.	17
Figure 6: Physical diagram of the adopted transceiver front-end.....	18
Figure 7: (a) The typical radiation pattern and the (b) typical relative spectral distribution of the infrared-based LED, (c) the relative sensitivity versus angle of incidence and (d) typical normalized frequency response of the	19
Figure 8: The concept diagram of the transceiver deployment and grid distribution	20
Figure 9: Location of the TX and measured areas in the production line scenario.	21
Figure 10: spatial properties of the OWC channel.	25
Figure 11: The (a) CIR of RX(2,0) and (b) RMS time delay when $Y=0$	26
Figure 12: measured average frequency responses in different RX location.	28
Figure 13: RT model and location-map of the TX and RX positions	29
Figure 14: multi-band power azimuth/azimuth profile in the LOS link TX1-RX1 in the machine room scenario. .	31
Figure 15: view from RX1 towards TX1 and the last interaction points of the identified MPCs in the link LOS TX1-RX1.	31
Figure 16: multi-band power azimuth/azimuth profile in the NLOS link TX1-RX4 in the machine room scenario.	32
Figure 17: view from RX4 towards TX1 and the last interaction point of the identified MPCs in the NLOS link TX1-RX4.	32
Figure 18: multi-band power azimuth/delay profile in the LOS link TX1-RX1 in the machine room scenario.	33
Figure 19: multi-band power azimuth/delay profile in the LOS link TX1-RX4 in the machine room scenario.	33
Figure 20: multi-band power delay profile in the LOS link TX1-RX1 in the machine room scenario.	34
Figure 21: multi-band power delay profile in the NLOS link TX1-RX4 in the machine room scenario.	34
Figure 22: polarimetric multi-band power azimuth/azimuth profile in the LOS link TX1-RX1 in the machine room scenario.....	35
Figure 23: polarimetric multi-band power azimuth/azimuth profile in the NLOS link TX1-RX4 in the machine room scenario.	36
Figure 24: multi-band delay spread in the machine room scenario.....	37
Figure 25: multi-band azimuth spread of arrival in the machine room scenario.	37
Figure 26: multi-band azimuth spread of departure in the machine room scenario.	38
Figure 27: (a) metal rack and (b) multi-band power azimuth/azimuth profile in the LOS link TX1-RX2 in the machine room scenario.....	39
Figure 28: multi-band synthetic omni-directional received power in the machine room scenario.	39
Figure 29: multi-band synthetic omni-directional path-loss in the machine room scenario.....	40
Table 1: channel sounder configuration in the industry hall scenario.....	15
Table 2: The detailed parameters of the transceiver	19
Table 3: measurement scenario definition.....	21
Table 4: 3D coordinates of the TX and RX locations in the production line scenario.	22
Table 5: The positional relationship of the transceiver	22
Table 6: 3D coordinates of the TX and RX locations in the machine room scenario.	29
Table 7: TX-RX link combination and visibility condition in the machine room scenario.	29
Table 8: channel sounder configuration for the sub-6 GHz, mmWave, and THz measurement campaign in the machine room scenario.....	30

Abbreviations

3GPP	3rd Generation Partnership Project
5G	Fifth Generation (mobile/cellular networks)
5G PPP	5G Infrastructure Public Private Partnership
6G	Sixth Generation Wireless Communication
6G BRAINS	Bringing Reinforcement learning Into Radio Light Network for Massive Connections
AP	Access Point
ASA	Azimuth Spread of Arrival
ASD	Azimuth Spread of Departure
AGV	Automated Guided Vehicles
BS	Base Station
CAD	Computer-aided Design
CIR	Channel Impulse Response
CNC	Computer Numerically Controlled
DMC	Dense Multipath Component
DoA	Direction of Arrival
DoD	Direction of Departure
DS	Delay Spread
eMBB	enhanced Mobile Broadband
FSPL	Free-Space Path Loss
IoT	Internet of Things
LED	Light Emitting Diode
LOS	Line-of-Sight
LSP	Large Scale Parameter

M2M	Machine to Machine
MISO	Multiple-single Multiple-Output
MLBS	Maximum Length Binary Sequence
mmWave	Millimeter-Wave
MPC	Multi-Path Component
NLOS	Non-Line-of-Sight
OWC	Optical Wireless Communication
PADP	Power Azimuth/Delay Profile
PCB	Printed Circuit Board
PD	Photodiode
PDP	Power Delay Profile
RF	Radio Frequency
RMS	Root Mean Square
RT	Raytracing
Rx	Receiver
SCM	Spatial Channel Model
SISO	Single Input Single Output
THz	Terahertz
ToF	Time of Flight
UE	User Equipment
mUE	Mobile User Equipment
SCM	Spatial Channel Model
SINR	Signal-to-Interference-Plus-Noise Ratio
SNR	Signal-to-Noise Ratio
TX	Transmitter
URLLC	Ultra-Reliable Low Latency Communications

V2V Vehicle-to-vehicle

VNA Vector Network Analyzer

WP3 Work Package Three

1 Introduction

Industry 4.0, as a typical industrial application of digital interconnection, plays a crucial role in the next generation of industrial manufacturing [SSH18]. It is envisioned that industry 4.0 based on wireless communications will facilitate significant advancements in the transformation of manufacturing and production processes. Meanwhile, industry 4.0 is also a major engine that triggers higher demands for the key performance indicators of the sixth generation (6G) wireless communication system [TSF21]. Specifically, it implies that wireless communications are confronted with increasingly stringent demands, including higher communication rates, extreme reliability connections, ultralow latency, and ultrahigh positioning accuracy. Although the phenomenal contribution achieved by radio-frequency (RF)-based communication technologies in the current information era has already been well established, the RF-based wireless networks are facing a looming crisis of spectrum shortage and increasingly serious electromagnetic interference. This calls for the use of augmentative technology and additional spectrum, with full spectrum communication emerging as a valuable solution. This includes sub-6 GHz, mmWave, THz and optical band-enabled communication [JSF23].

Since the low-frequency band has been widely used in 2G, 3G, and 4G mobile communications, while the mmWave and higher-frequency bands are primarily undergoing experimental exploration, the middle-frequency band (roughly in the 3-6 GHz), which is referred to as the sub-6 GHz band, stands out as the most prominent frequency range for 5G mobile communication [SSB19]. Thus, existing techniques, such as multiplexing URLLC and eMBB services discussed by 3GPP, primarily focus on achieving URLLC exclusively within the sub-6 GHz frequency range. In other words, communication based on the sub-6 GHz band still plays an indispensable role in Industry 4.0. However, due to the limited spectrum resources within the sub-6 GHz range, it is essential to make full use of mmWave, THz, and optical bands [WWL19].

Thanks to the promising spectrum availability, mmWave communication stands out as a critical facilitator for eMBB applications. The implementation of compact antenna arrays with a large number of elements can be achieved based on mmWave frequency bands. This capability supports pencil-beam directional transmissions and extends the transmission range, which is especially appealing for small-scale industrial control equipment requiring both URLLC and high data rates. Moreover, strategically deploying mmWave cells within the communication coverage areas can effectively eliminate coverage gaps, offload traffic, provide high data rates, and reduce over-the-air transmission latency. These unique characteristics also position mmWave communication as a crucial enabler for rapid wireless backhaul connectivity, particularly in ultra-dense network deployments. However, mmWave signals cannot easily penetrate obstacles, resulting in highly intermittent mmWave links [RRE14]. This presents a significant challenge for wireless applications in complex industrial environments. Fortunately, obstacles in industrial scenarios typically have fixed positions and directions. Consequently, studying the channel characteristics of mmWave in industrial settings is crucial for establishing high-reliability communication within the mmWave frequency range.

Despite mmWave bands offer spectral redundancy, they may not prove adequate to address the increasing demand for bandwidth in the coming decade. THz is considered a promising candidate to achieve Tbps communications using current wireless communication processing

technologies and hardware capabilities. In other words, Tbps communications can be attained through the utilization of the abundant frequencies above 100 GHz [RXK19]. Moreover, since the spatial resolution of wireless signals is proportional to the operating frequency, THz-based positioning and imaging can achieve higher resolution and penetration capability without significant environmental interference and ionization by utilizing its tiny wavelength on the order of micrometres and frequency-selective resonances [MMN18]. Similar to the propagation characteristics of sub-6 GHz and mmWave, THz signal also experiences free-space path loss (FSPL) due to the inherent attenuation produced by isotropic antenna aperture. It is noted that the receiving antenna in the THz wireless communication has limited capability to capture radiation power because of the extremely small isotropic antenna aperture. This results in FSPL in THz band being more pronounced.

Optical wireless communication (OWC) can smoothly meet a wide range of communication and positioning service demands by utilizing its extensive spectrum resources, including infrared, visible light, and ultraviolet light. Moreover, OWC technology is expected to be applied in the industry 4.0 revolution that provides massively connected and highly reliable wireless communication and sensing networks. In industrial environments, there is a significant amount of lighting infrastructure that facilitates the rapid deployment of OWC systems. Meantime, numerous electrical devices already support infrared transmission, enabling seamless integration of OWC networks with existing facilities. Due to the fundamental effect of the channel model, numerous works have been devoted to investigating the channel model of sub-6 GHz, mmWave, THz, and OWC system. These channel model can be divided into deterministic and stochastic modelling approaches. The deterministic channel models heavily depend on the detailed information of specific propagation scenario, as well as the position and angle between the transceivers. Consequently, the achievable channel model is more accurate within the same scenario but less adaptable to different scenarios. Meantime, since the accuracy of the channel gain increases with the computable bounce number and reflection unit, it is worth to achieve accurate channel information with an acceptable computing cost. Moreover, the stochastic approach is modelled by statistical distribution and probability theory. Benefiting from this, the stochastic approach offers greater flexibility and lower computational complexity but at the expense of channel accuracy when compared to the deterministic channel. On the other hand, several works have been carried out to investigate the channel model from the experimental level. Thus, this document focuses on multi-band channel measurements and analysis in both laboratory and industrial environments, including sub-6 GHz, mmWave, sub-THz, and optical bands. The multi-band wave propagation measurements including different frequency bands from sub-6 GHz, mmWave and THz up to the optical spectrum. The new multiband RF measurements were expanded including an optical component with at least 200 MHz bandwidth.

2 Scenarios

2.1 Machine Room

This scenario corresponds to a laboratory room located in the Fraunhofer facilities in Ilmenau, Germany. The dimensions of the room are 6.48 m × 10.05 m × 6.33 m and there are different tools typically found in industrial and machine halls, as shown in the 360° pictures taken from one of the TX and one of the RX positions in Figure 1, respectively. The predominant constructive materials of the different items are iron, steel, aluminium, plexiglass, concrete, and steel sheet. This scenario can be easily compared to a portion of a production line. The main component in the room is a computer numerically controlled (CNC) milling machine located in the centre of the room.



(a)



(b)

Figure 1: picture of the machine room scenario taken by the channel sounder (a) TX, and (b) RX.

2.2 Industry Hall

The industrial hall scenario is part of the BOSCH factory in Blaichach, Germany. This scenario was already presented in detail in the deliverable D3.1. The complete hall has a size of 74 m x 171 m x 11 m, however the measurements were conducted in a portion of 46 m x 42 m x 11

m, as indicated in the Figure 2. The main constructive materials are steel, concrete, glass, aluminium, etc. In the measured area, there are 2 production lines and a large storage area, as shown in the picture from the TX shown in Figure 3.

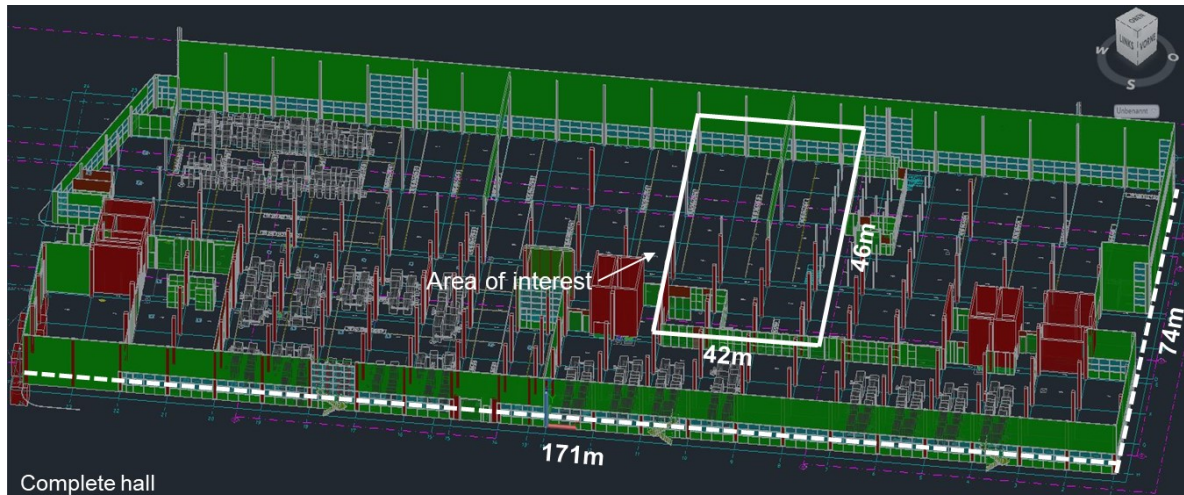


Figure 2: schematic of the industrial hall at BOSCH in Blaichach.



Figure 3: composite picture from the channel sounder (TX) towards the measurement area in the industry hall scenario.

3 Multiband Sub-6 GHz and mmWave Propagation Measurements and Analysis Results in Large Industrial Scenario

More details on this measurement campaign and the results can be found in [DHE22].

3.1 Measurement Set-up

The measurements emulate a scenario of an antenna located in the top of a production unit connected to a 5G gateway supporting the complete production cell. The multi-band channel sounder simultaneously measures up to three different bands with a null-to-null measurement bandwidth of 6.75 GHz.

The measured centre frequency of the different bands were 6.75 GHz (covering the sub-6 GHz spectrum), 33.75 GHz, and 60.75 GHz (labelled as 30 GHz and 60 GHz for sake of simplicity). The excitation signal of the baseband units was a 15-bit maximum length binary sequence (MLBS), covering an unambiguity range in propagation distance of ≈ 1455 m.

The sounder consists of a single TX unit and two different RX units located in different positions that measure in parallel the three bands. The angular domain was scanned at the TX using 30° half-power beamwidth (HPBW) horn antennas mounted over a positioner at 4.2 m height (above clutter level) scanning from -90° to 90° in azimuth and from -60° to 30° in elevation with 30° steps. A single horn antenna was used for the sub-6 GHz and the 30 GHz bands, and a different one located 4 cm below, for the 60 GHz band. On the other side, omnidirectional antennas were used at the RX to save measurement time and collect more positions for statistics. A single custom antenna was used for the sub-6 GHz and 30 GHz bands, and a separated dipole for the 60 GHz band. Both antennas were located at 1.36 m height, separated 0.5 m over a rotational joint. After the TX carried out a complete scan in the angular domain, the RX antennas were rotated in such a way that the sub-6 GHz and 30 GHz antenna takes the place of the 60 GHz antenna, and vice-versa. Hence, after two scans take place in the angular domain at the TX, we have two different measurement points separated 0.5 m at the RX. All these details are summarized in Table 1.

Table 1: channel sounder configuration in the industry hall scenario.

	Sub-6 GHz	mmWave	mmWave
Central frequency	6.75 GHz	33.75 GHz	60.75 GHz
Label	Sub-6 GHz	30 GHz	60 GHz
M-Sequence length	4095		
Bandwidth (null-to-null)	6.75 GHz		
TX antenna (HPBW)	30°		
RX antenna (HPBW)	Isotropic		
TX azimuth scans	-90° to 90° with 30° steps		

TX elevation scans	-60° to 30° with 30° steps
RX azimuth scans	0°
RX elevation scans	0°

The RX was located over 4 different tracks with 0.5 m separation between measurement positions as shown with green markers for the LOS and red for the NLOS in Figure 4: location of the RXs in the industry hall scenario.. The position 0 starts in the bottom line of the figure. However, due to different reasons as people or vehicles passing by, some of the marked positions were not included in the analysis.

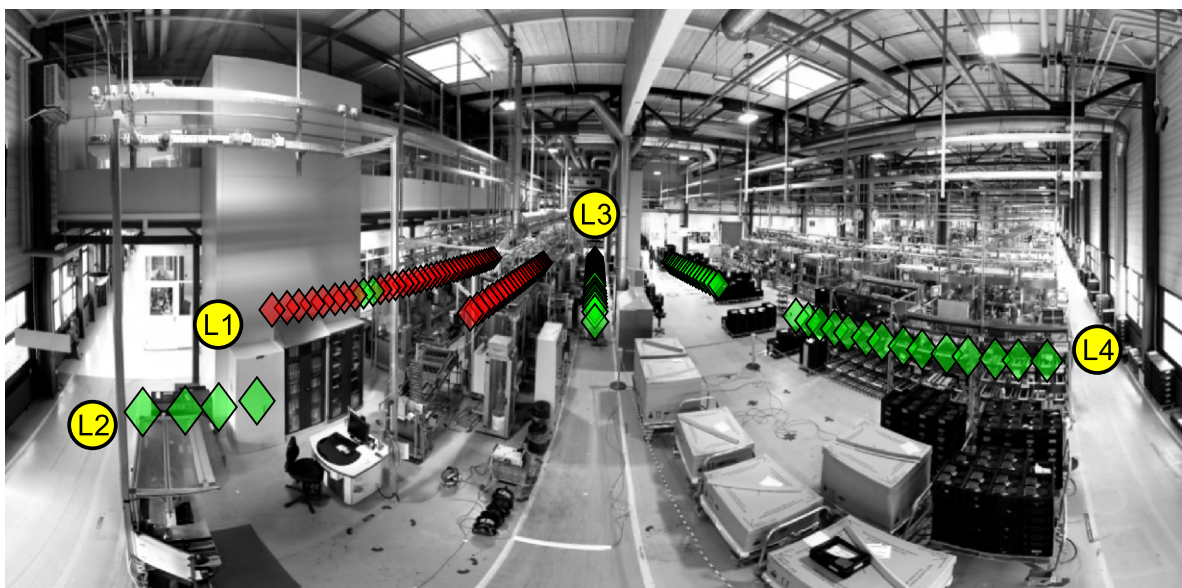


Figure 4: location of the RXs in the industry hall scenario.

3.2 Temporal Properties of the Propagation Channel

The multi-band isotropic PDPs over the measured track L1 in NLOS and track L3 in LOS with the different bands are shown in Figure 5. The propagation distance (delay multiplied by the propagation speed of light in vacuum) is used for a better interpretation of the source of the MPCs.

The same strong dominant paths (presumably from specular reflections) can be observed along the sub-6 GHz and mmWave bands, as observed in previous measurements with the same channel sounder [DMS19, DML19, DML20] and from independent researchers [HLZ22].

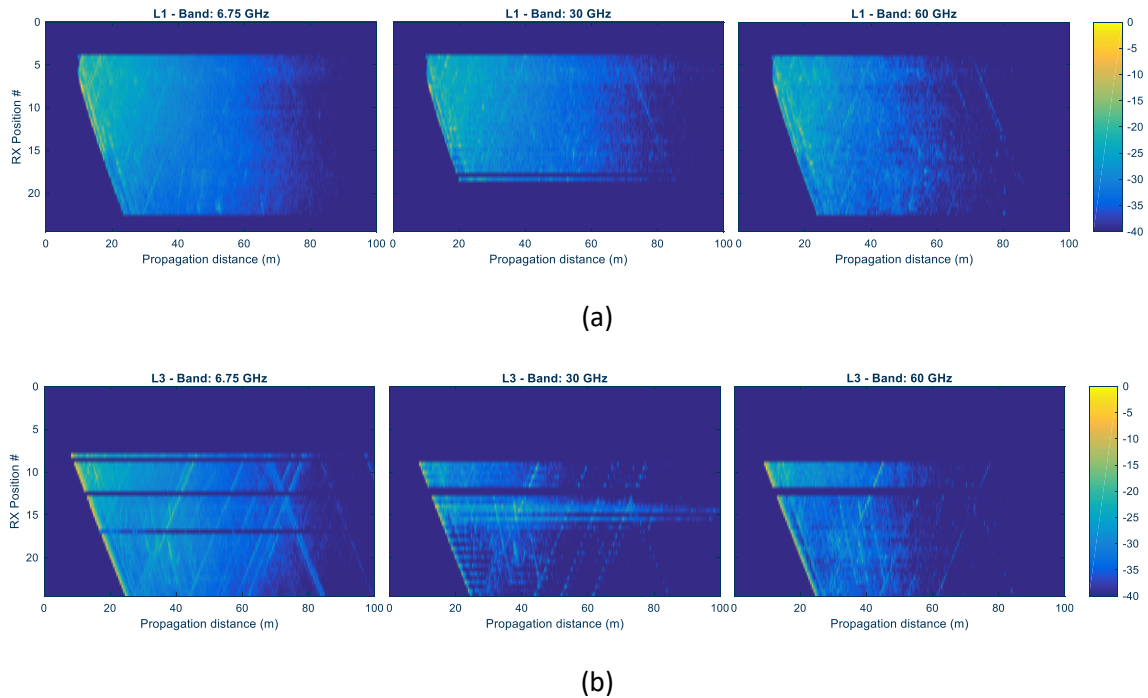


Figure 5: multi-band isotropic PDP over the different positions in (a) L1 in NLOS and (b) L3 in LOS in the industry hall scenario.

3.3 Large-Scale Parameters

Due to the measurement set-up based on directional scans with high gain antennas at the TX and no spatial resolution at the RX, only the following LSPs are possible to be characterized: DS, ASD, and ESD.

3.4 Conclusions

The analysis of the synthetic omni-directional PDPs of the multi-band measurement has shown that the dominant paths are present with similar gain in the different bands. In addition, the channel is not as sparse as it is usually expected and a large amount of DMC power was observed also in the mmWave bands. These results are consistent with previous work presented in similar industrial scenarios in [DML20], in indoor scenarios in [DMS19] and from other researchers in V2V measurements in [HLZ22].

4 OWC Channel measurement and analysis results

4.1 OWC front-end description

In the OWC channel measurement, an infrared band-based (700nm~1000nm) transceiver front-end designed by OLEDCOMM was exploited to measure the OWC channel in the practical factory at BOSCH.

Figure 6 shows the physical diagram of the Tx front-end. The infrared-based LED Tx and the PD-based receiver are uniformly integrated into the one PCB board. Moreover, the network port, as the only interface of the transceiver, provides 12V direct current power supply and data transmitting for the transceiver. The typical radiation pattern and the typical relative spectral distribution of the infrared-based LED is shown in Figure 7(a) and (b). The peak wavelength is at 945nm and the full width at half maximum spectral width is 45nm. Meanwhile, Figure 7(c) and (d) depicts the relative sensitivity versus angle of incidence and (d) typical normalized frequency response of the PD. The semi-angle at half-sensitivity is at 62° and the 3 dB bandwidth of the PD is 50MHz. The other parameters were summarized in Table 2.

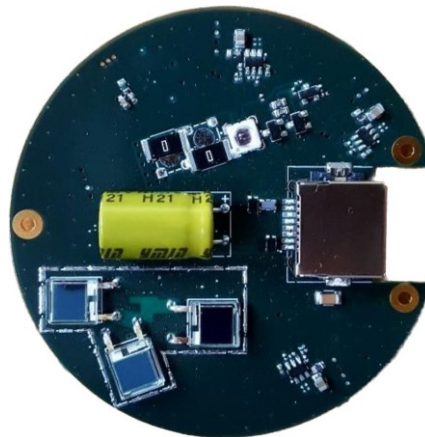
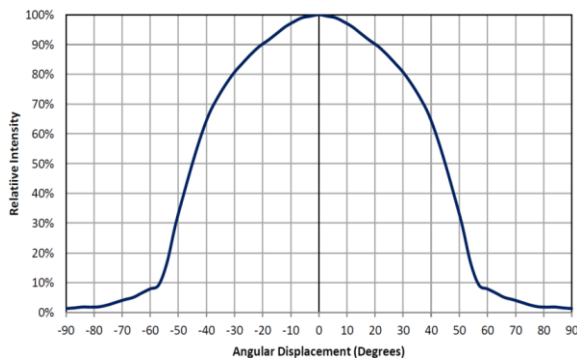
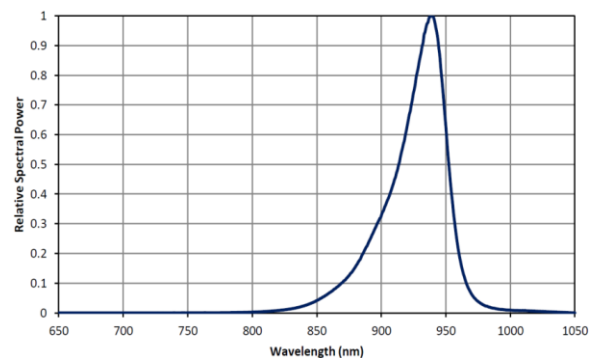


Figure 6: Physical diagram of the adopted transceiver front-end.



(a)



(b)

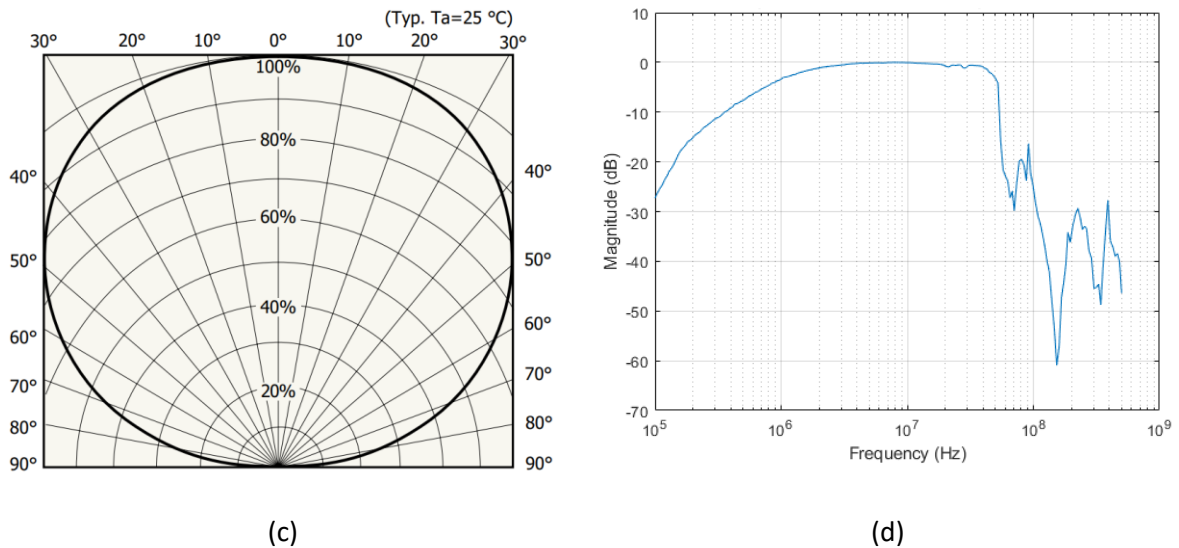


Figure 7: (a) The typical radiation pattern and the (b) typical relative spectral distribution of the infrared-based LED, (c) the relative sensitivity versus angle of incidence and (d) typical normalized frequency response of the

Table 2: The detailed parameters of the transceiver

Tx		Rx	
Item	Value	Item	Value
Lambertian mode (m)	1	Effective sensitive area	79.2 mm ²
Elevation	-90°	Elevation	+90°
Azimuth	0°	Azimuth	0°
Semi-angle at half power	45°	Sensitivity range	320 nm – 1060 nm
LED drive current range	350 mA ± 250 mA	Typical sensitivity	0.65A/W@ 900 nm
LED optical power range	472.5 mW ± 337.5 mW	Semi-angle at half-sensitivity	62°

4.2 Measurement Set-up

The measurement was conducted in the factory hall scenario. Considering that the OWC channel gain is directly related to the distance between the LED-based TX and the PD-based RX a transceiver as the infrared LED-based TX was fixed at a specific location in the area to be measured, while another transceiver as the PD-based RX was moved in the receiving plane

[ADT21, AWZ18, BSH18]. For the convenience of statistics and analysis, the receiving plane was evenly divided into multiple grids, which the size of the grid was set as $0.2 \times 0.2 \text{ m}^2$. The concept diagram of the TX and RX deployment and grid distribution is shown in Figure 8. In order to provide best possible communication services and improve the communication coverage area, the Tx front-end was tilted 45° instead of facing vertically towards the ground. On the contrary, considering that the RX may be positioned in multiple locations within the industry hall scenario the RX front-end was set up vertically facing the ceiling to facilitate subsequent data analysis. Moreover, in view of the practical conditions of the industry hall environment and the production line operating platform and the instruments involved, the height of the TX front-end and RX front-end were fixed at 2.9m and 1.1m, respectively.

Following the deployment and setup shown in Figure 8, the OWC channel measurement was performed at the production line 8 of the BOSCH factory in Blaichach, Germany. Figure 9 depicts the location of the Tx and measured area in the production line scenario. Specifically, eight measurement areas were chosen based on the practical conditions and 10 measurements were performed. The measurement number of 2 and 3, as shown in Figure 9, were time-sharing measurements to evaluate the channel characteristics of multiple Txs. Thus, there are nine measurement scenarios were considered in this OWC channel measurement. The characteristics of these scenarios were listed in the Table 3.

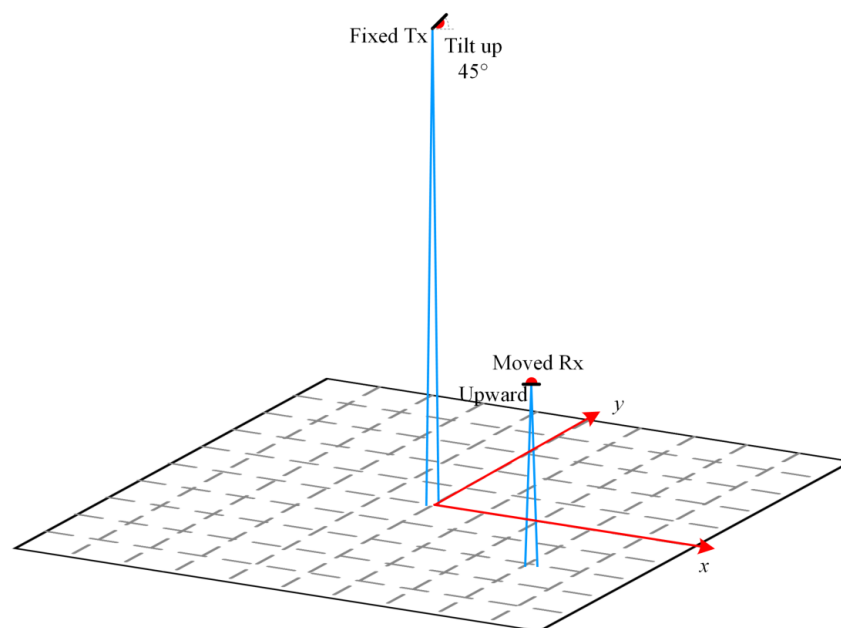


Figure 8: The concept diagram of the transceiver deployment and grid distribution

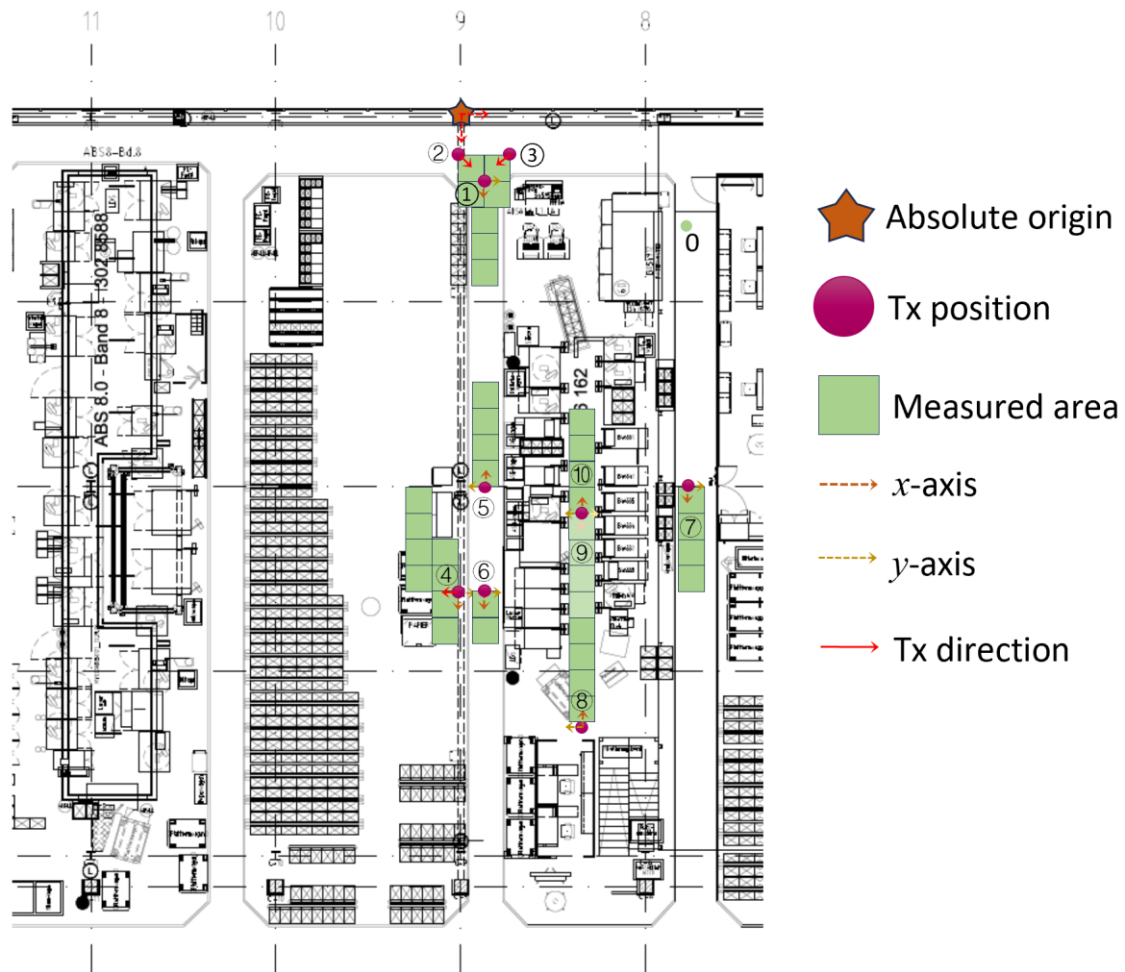


Figure 9: Location of the TX and measured areas in the production line scenario.

Table 3: measurement scenario definition

Scenario definition	Characteristic	Location in Figure 9
Scenario 1	A at the upper left corner of the production line and the clear white windows which outdoor ambient light can penetrate.	①
Scenario 2	Two LED-based TXs are respectively deployed at two corners of the grid near the window. This scenario is measured to investigate the multiple input single output (MISO) OWC channel characteristic.	② ③
Scenario 3	Supermarket, namely material storage area, where the automated guided vehicles (AGV) places production materials. Since materials and production facilities are in and around the supermarket, we choose an area without materials based on the actual scenario to ensure the normal operation of the production line. Thus, the measurement area is irregular shape, as shown in table 5.	④
Scenario 4	Close to the back of the production line machine and there are two cement pillars on the left side of the area	⑤

Scenario 5	The left side of the area is the supermarket scenario, and the right side is the back of the production line machine.	⑥
Scenario 6	There is a moving rail above this area, the height of which is lower than the Tx. Moreover, there is a row of lockers to the left of the measurement area.	⑦
Scenario 7, 8,9	Located in the middle of the production line, workers mainly move in this area and control the operation table. Due to the limited coverage of LED emission, we divided the internal space of the production line into three scenes, and the deployment of the three scenes was roughly equal.	⑧,⑨,⑩

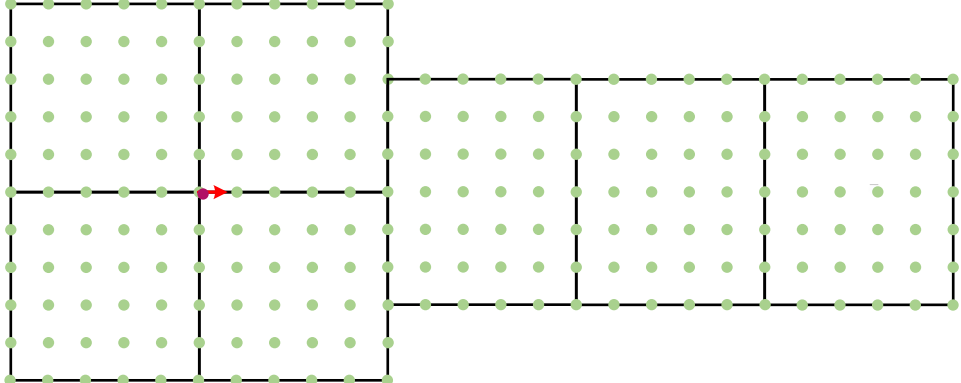
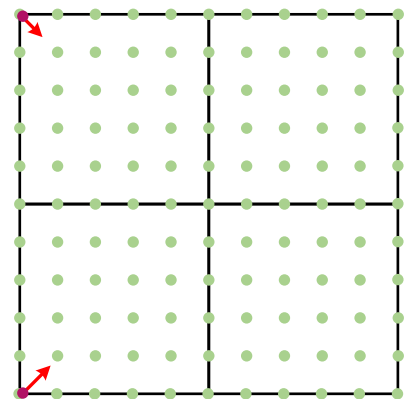
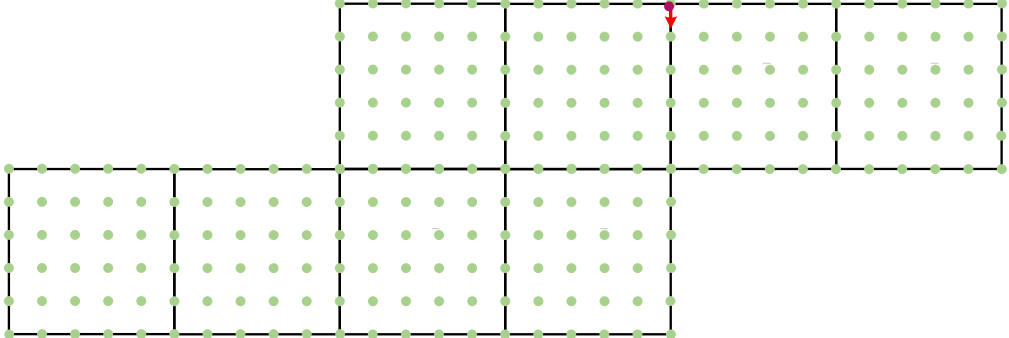
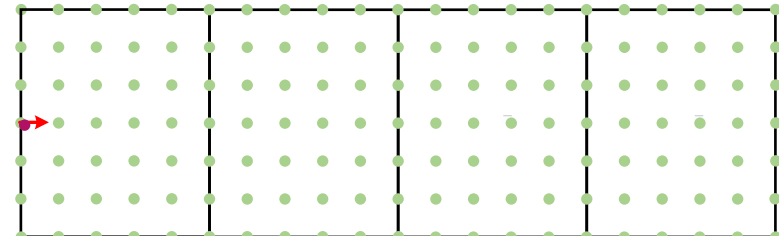
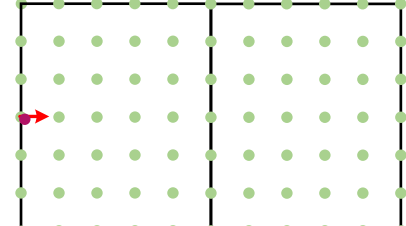
In the considered nine scenarios, we selected one TX (namely TX1, and Tx 4 - -Tx 10) in each of the scenarios 1, and 3-9 and deployed two TXs (namely TX2 and TX3) in scenario 2 based on a time-sharing method. Moreover, since there may be interference from inherent noise and environmental noise in the communication link, it is necessary to determine these noises and subtract them in the VNA as background noise during the channel measurements. Thus, the corresponding precise location coordinates of the TXr and RX in the scenario are listed in Table 4. Specifically, the orange star in figure 9 was defined as the absolute origin during this OWC channel measurement, and RX 0 (RX0 marked in Table 4) is adopted to measure the background noise across the communication link. The principle of selecting this location was to minimize the influence of LOS and NLOS links. For other RX coordinates of the measurement scenario, they were distributed in a square area (number 1 as shown in Figure 9) with the TX as the origin or a rectangular area (number 4-10 as shown in Figure 9) with the axis of symmetry. Thus, other RX location was not listed in Table 4 for brevity.

Table 4: 3D coordinates of the TX and RX locations in the production line scenario.

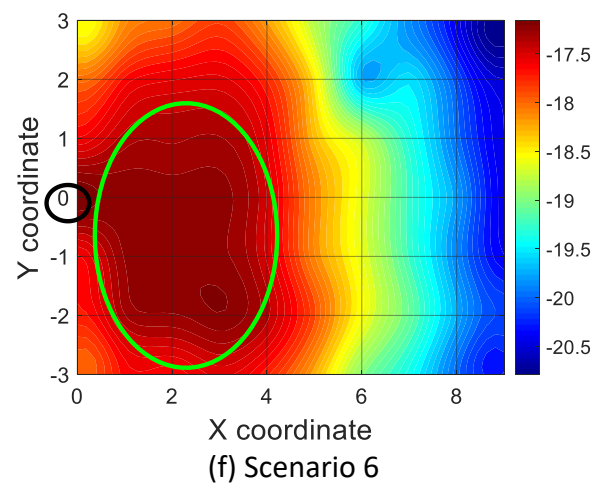
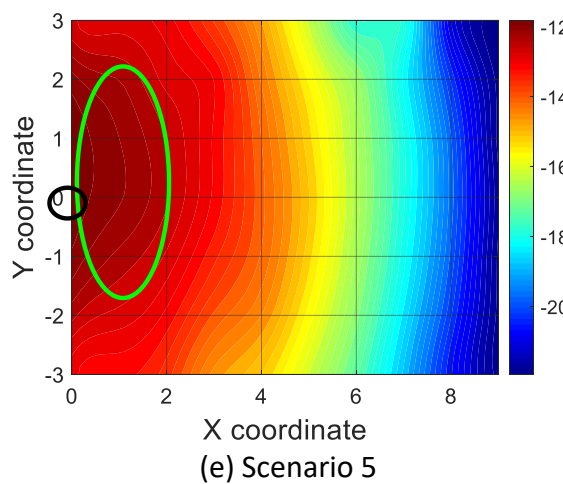
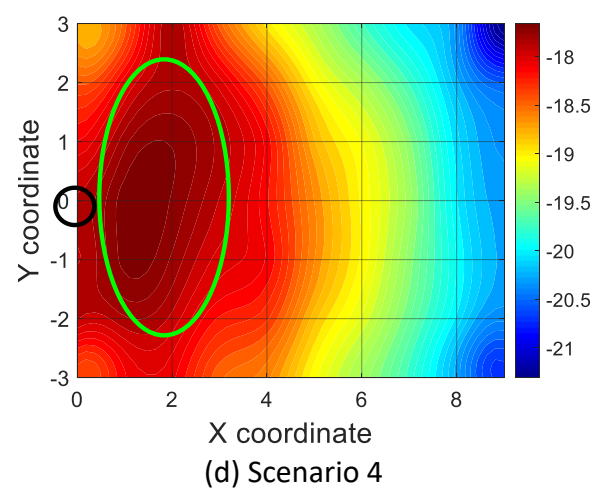
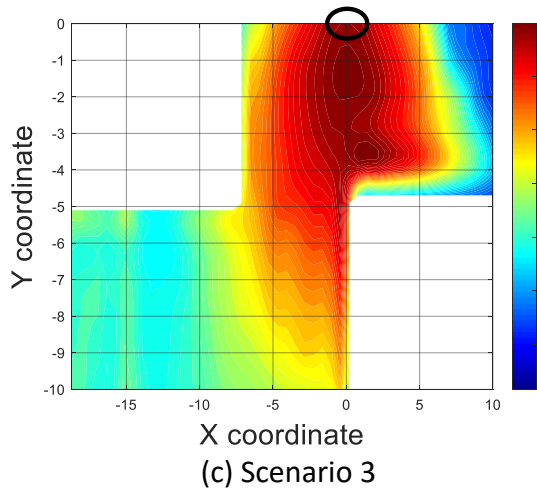
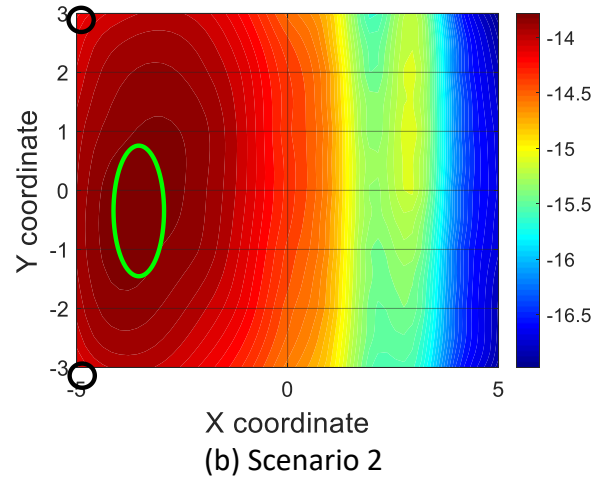
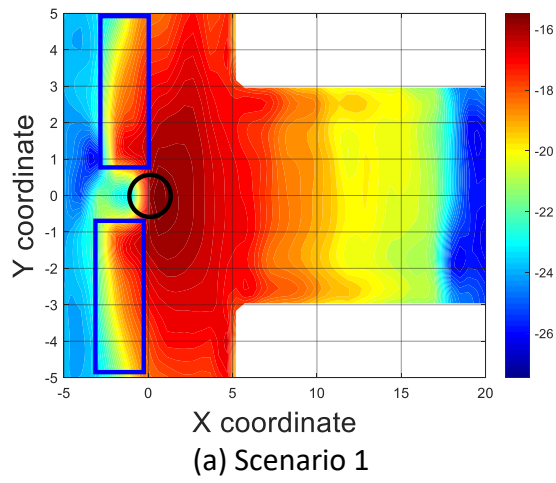
	TX1	TX2	TX3	TX4	TX5	TX6	TX7	TX8	TX9	TX10	RX0
x (m)	2.68	1.68	3.68	17.03	12.95	17.03	23.23	15.23	15.23	14.23	4.25
y (m)	0.8	-0.2	1.8	0.2	0.8	0.8	4.57	4.57	4.57	8.5	7.9
z (m)	2.9	2.9	2.9	2.9	2.9	2.9	2.9	2.9	2.9	2.9	1.1

In order to further elaborate on the positional relationship of the TX and RX, Table 5 shows the r location distribution in the considered nine measurement scenarios. Note that the red dot indicates TX and green dot represents RX, and the red arrow indicates orientation of TX in azimuth.

Table 5: The positional relationship of the transceiver

<p>Scenario 1</p>	
<p>Scenario 2</p>	
<p>Scenario 3</p>	
<p>Scenario 4,6,7,8,9</p>	
<p>Scenario 5</p>	

4.3 Spatial Properties of the Propagation Channel



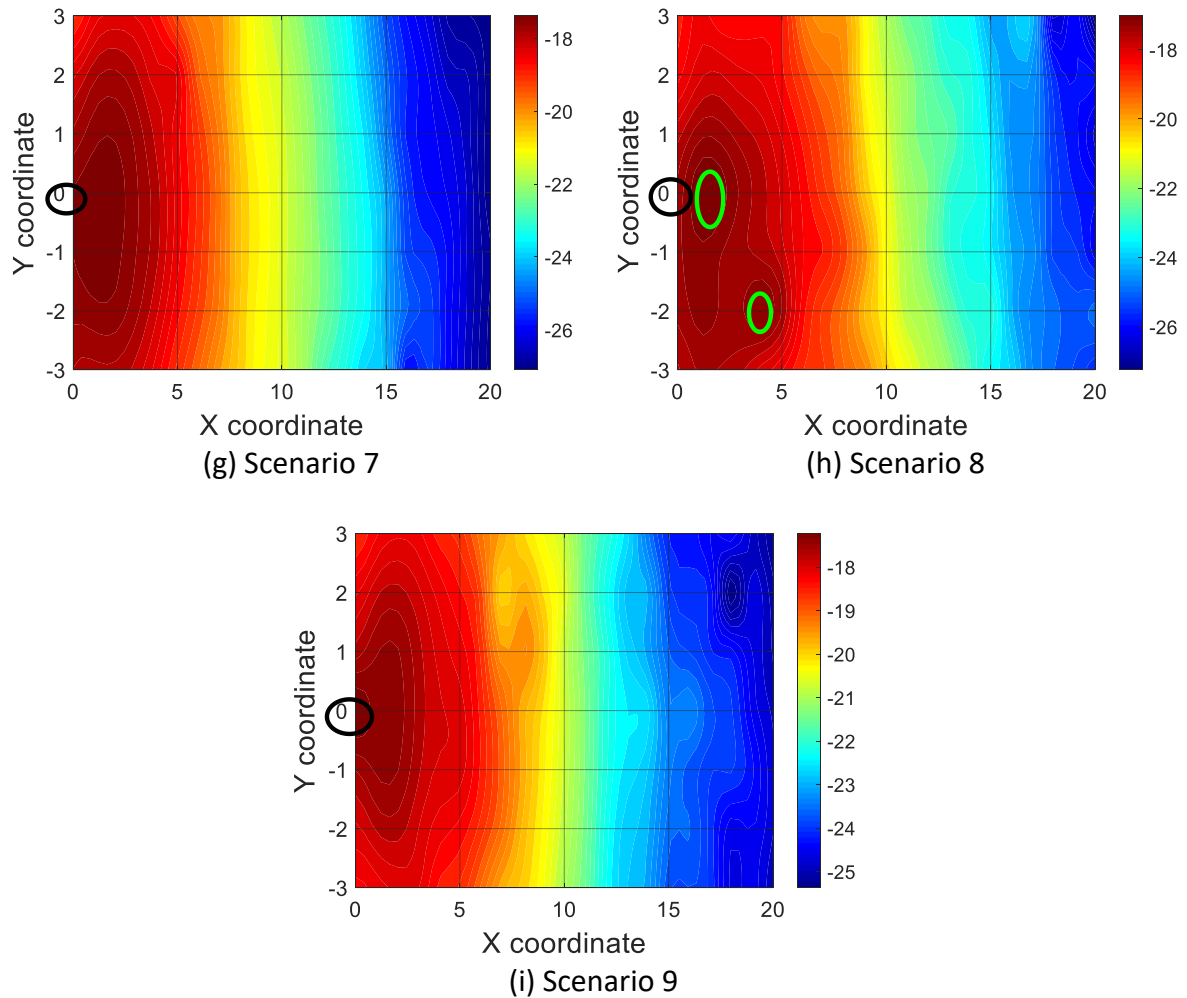


Figure 10: spatial properties of the OWC channel.

Figure 10: spatial properties of the OWC channel. depicts the spatial properties of channel gain in these considered scenarios, where the X and Y coordinates are in meters. Specifically, Figure 10 (a)-(i) are to the channel link fading intensity diagrams of scenarios 1-9, respectively. Due to the actual constraints of the scenario, the white area in the Figure 10(a) and (d) indicates the unmeasured area. Moreover, the black circle marks the location of the Tx, which is the origin of the diagram.

It can be seen from the result of scenario 1 that the channel gain in the area within two meters directly in front of the Tx is better. Moreover, the channel in the back area of the Tx, that is, the pink rectangular area, also has a strong gain. This is because the optical radiation follows the Lambertian model, and the Tx is tilted upward at 45°. For the scenario 2, the area with the strongest channel gain is located between the two Txs. It also can be seen that the channel gain distribution in the MISO scenario is stronger and more uniform than the channel gain distribution in the same area in Scenario 1.

Figure 10: spatial properties of the OWC channel.(c) shown the channel gain distribution of the supermarket scenario. It can be seen that compared with the other scenarios, the area where the channel gain intensity is red is smaller. In other words, the high channel gain distribution of the scenario 3 is narrower in the X-axis direction. This is because the measurement area of scenario 4 is an open area without materials, and the height of the

surrounding baskets containing production materials is lower than the height of the receiver, such that the channel gain in this scenario is less affected by NLOS links. Thus, the beam in this scenario has better directionality. Moreover, based on the above facts, the channel gain was rapidly attenuated in the areas (cyan region) far from the Tx.

Since scenario 4, 5, and 6 are similar, which are located at both ends of the production line, we focused on comparing and analysing the result of Figure 10(d), (e), and (f). Although the scenario 3 and 6 respectively collected measurement data within a $4 \times 1 \text{ m}^2$ region, the channel characteristics of the first $2 \times 1 \text{ m}^2$ region of scenarios 3 and 6 were analysed such that it can be more intuitively compared with scenario 5. Compared with Figure 10(e), it can be observed that the region of strong channel gain in both Figure 10(d) and (f) is wider, especially the strong channel gain area in Figure 10(f) is the largest. This can be explained by the fact that there are more NLOS links in both scenario 3 and 6, and those NLOS links can contribute to the overall channel gain. Moreover, since cement pillars locate on the left side of the scenario 3, more high channel gain links are concentrated in the upper half of the y-axis area as shown in Figure 10: spatial properties of the OWC channel.(c). Similarly, due to the existence of the lockers on the left of scenario 6, more high channel gain links are concentrated in the lower half of the y-axis area as shown in Figure 10(f). However, since the tilt angle of the Tx is less than 45° in scenario 5, the maximum channel gain of scenario 5 is higher than that of both scenarios 3 and 6. Meantime, compared to scenarios 3 and 6, the region of high channel gain in scenario 5 is closer to the Tx.

Figure 10 (g), (h), and (i) depict the channel gain distribution of scenario 7, 8, and 9, respectively. Note that these three scenarios were located in the middle of the production line. Since both sides of the three scenarios were covered with equipment, the NLOS components in those scenarios were more abundant than in other scenarios. This can be verified by the larger area of the red region in Figure 10(g) - (i) compared to other scenes. In particular, the scenario 8 was located in the middle area inside the production line, such that the OWC channel environment is the most complex. As a result, there are two small areas where the channel gain can reach -17dB .

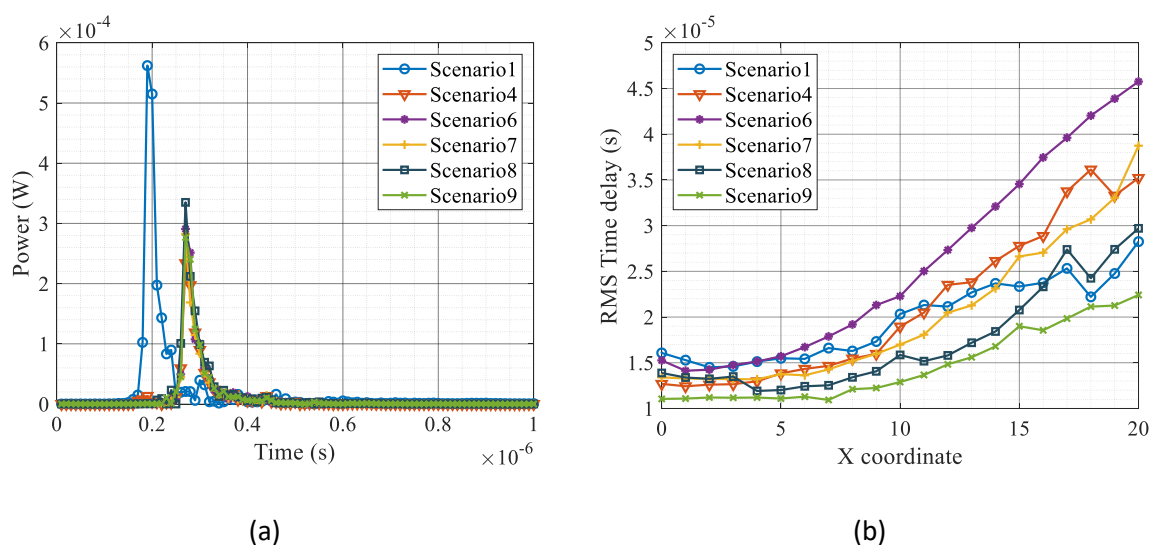
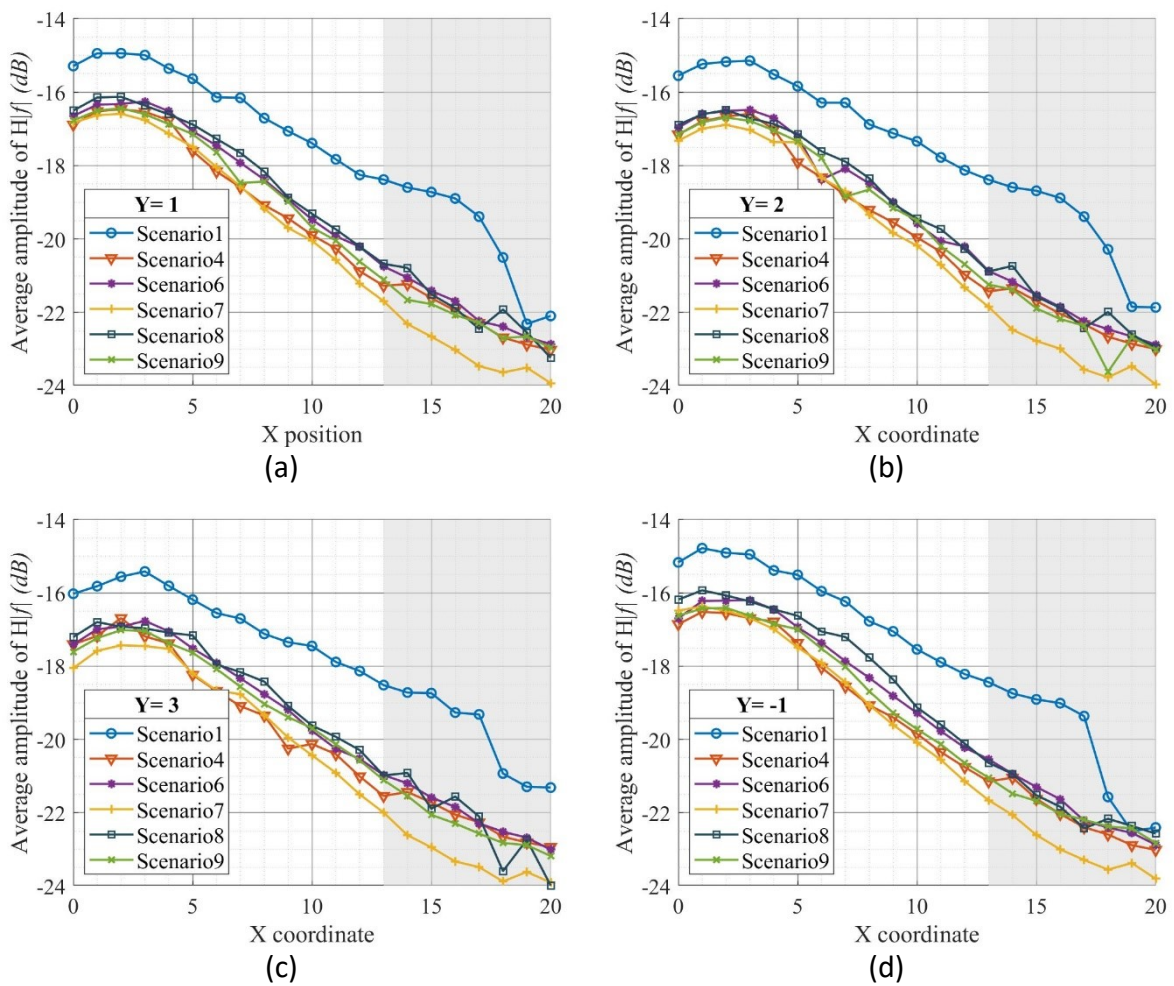


Figure 11: The (a) CIR of RX(2,0) and (b) RMS time delay when Y=0

Based on the above analysis, the scenarios 1, 4, and 6-9 are selected for further investigation. Due to the similarity, the CIR of the receiver at coordinate (2,0) and the RMS time delay of all points with $Y=0$ in each scenario is analysed, as shown in Figure 11. Different from the simulation level, the channel propagation time includes not only free space transmission time, but also device and cable transmission time. Thus, the time corresponding to the peak value of the received signal is greater than a few nanoseconds. Moreover, since a short network cable is adopted in the scenario 1, its time is shorter than that of other scenarios. Furthermore, Figure 11 shows that the impact of multipath dispersion between transceiver is more pronounced in the scenario 6 compared to other scenarios. The reason is that the hollow conveyor belts closer to the Tx result in more multipath variability.



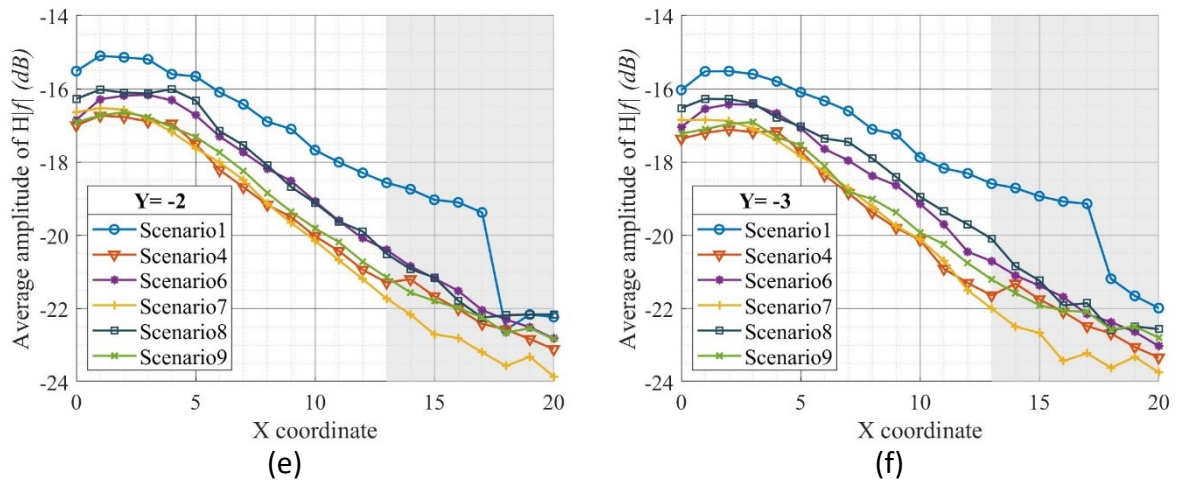


Figure 12: measured average frequency responses in different RX location.

Finally, Figure 12 depict the measured average frequency responses of the receivers with different Y value. Based on the changing trends of these curves, the measured area can be divided into two parts. In the first 2.6 m area in the X-axis direction, the strong LOS link dominates the channel, and the channel gains fluctuate slowly, while the NLOS links significantly affects channel and the corresponding channel gains fluctuate strongly in the following 1.4 m area.

5 Multiband Sub-6 GHz, mmWave, and sub-THz Propagation Measurements and Analysis in Machine Room

5.1 Measurement Set-up

Two different TX and 10 different RX positions were measured in LOS and NLOS visibility conditions. The precise location coordinates of the TXs and RXs in the scenario are listed in Table 6 and shown in the map in Figure 13.

Table 6: 3D coordinates of the TX and RX locations in the machine room scenario.

	TX1	TX2	RX1	RX2	RX3	RX4	RX5	RX6	RX7	RX8	RX9	RX10
x (m)	4.03	5.53	4.01	4.51	5.01	5.51	4.01	4.51	5.1	4.01	4.51	4.01
y (m)	4.99	4.24	8.44	8.44	8.44	8.44	11.94	11.94	11.94	11.19	11.19	10.44
z (m)	1.72	1.72	1.72	1.72	1.72	1.72	1.72	1.72	1.72	1.72	1.72	1.72

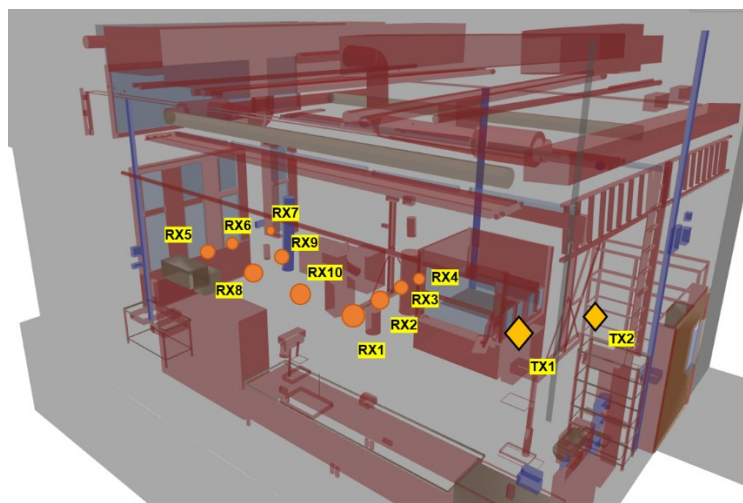


Figure 13: RT model and location-map of the TX and RX positions

However, not all the combinations of TX and RX were measured. The list of measured links and the visibility condition is displayed in Table 7.

Table 7: TX-RX link combination and visibility condition in the machine room scenario.

	RX1	RX2	RX3	RX4	RX5	RX6	RX7	RX8	RX9	RX10
TX1	LOS	LOS	LOS	NLOS	LOS	LOS	NLOS	LOS	LOS	LOS
TX2	LOS	-	-	-	NLOS	NLOS	NLOS	-	-	-

The detailed description of the channel sounder used in this measurement campaign and its calibration has been introduced in the deliverable D3.2. The configuration of the channel sounder parameters for the different bands can be found in Table 8.

Table 8: channel sounder configuration for the sub-6 GHz, mmWave, and THz measurement campaign in the machine room scenario.

	Sub-6 GHz	mmWave	THz
Central frequency	6.75 GHz	74.25 GHz	187.5 GHz
Label	Sub-6 GHz	70 GHz	200 GHz
M-Sequence length	4095		
Bandwidth (null-to-null)	6.75 GHz		7.5 GHz
Bandwidth (after FR calibration)	5 GHz		
TX antenna (HPBW)	30°	15°	
RX antenna (HPBW)	30°	15°	
TX azimuth scans	-180° to 165° with 15° steps		
TX elevation scans	0°		
RX azimuth scans	-180° to 165° with 15° steps		
RX elevation scans	0°		

5.2 Spatial Properties of the Propagation Channel

The power bi-azimuth profiles at sub-6 GHz, mmWave, and THz for the LOS position are shown in the following figures.

Apart from the LOS component in the TX and RX scanning direction 0° (marked as *A*), there are two other strong components visible in the different bands (white circles): a reflection in the milling machine at TX scanning direction 30° and RX scanning direction -30° (marked as *B*), and a reflection in the wall at TX and RX scanning directions -60° and 60°, respectively, marked as *C*. In addition, at sub-6 GHz and mmWave (yellow circles), there are other clusters visible in the TX 150° and RX -15° scanning directions (reflection from the wall located in the rear part of the TX channel sounder) and from TX 0° and RX -180° (metal frames from door in the rear part of the RX). These components are not visible at THz most probably due to the limited dynamic range of the measurement equipment. Moreover, some other clusters are identified at sub-6 GHz and not present in the mmWave or THz bands (red circles).

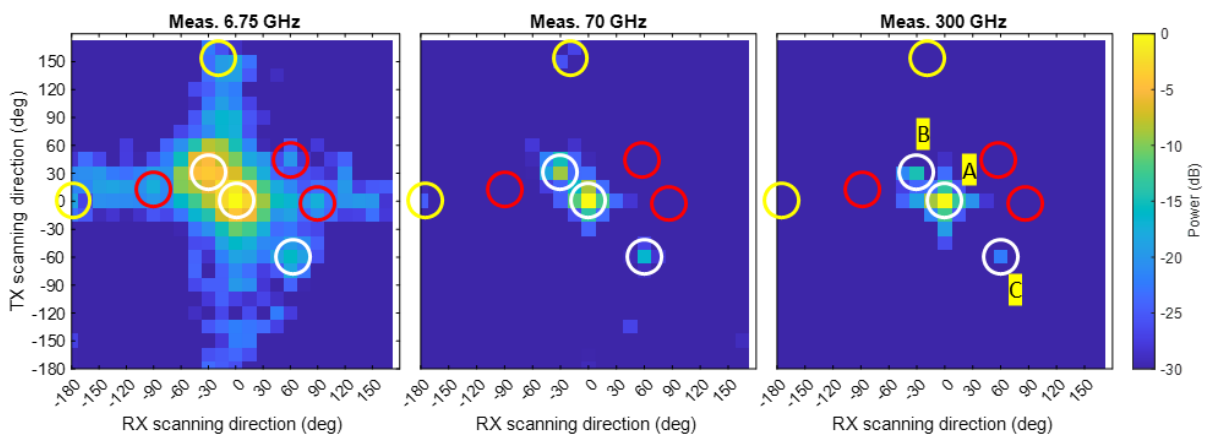


Figure 14: multi-band power azimuth/azimuth profile in the LOS link TX1-RX1 in the machine room scenario.

Using the TX and RX scanning directions, and the propagation distance of the path (observed in the power delay profiles), the clusters are identified in the picture 360° taken in the positions of the channel sounder, displayed in Figure 15.

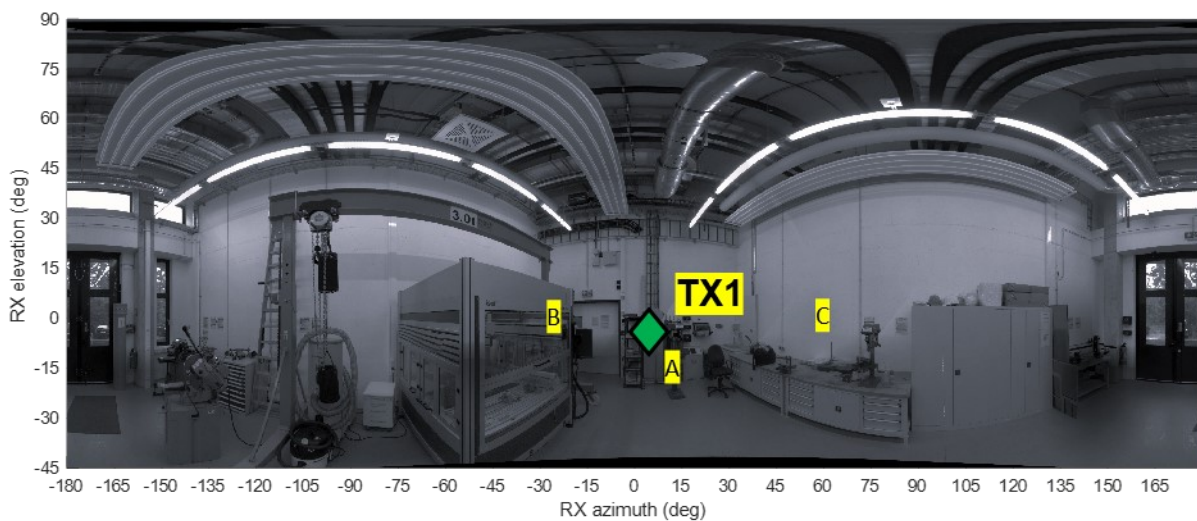


Figure 15: view from RX1 towards TX1 and the last interaction points of the identified MPCs in the link LOS TX1-RX1.

Similarly, in NLOS, there are also many clusters visible in all the measured bands and some others visible only at lower frequencies as shown in Figure 16. Due to the lack of the LOS component, many more clusters appear within the considered dynamic range. High order reflections in the THz band were identified in cluster A (cupboard and metal frame of the doors), B (reflections from the metal frames of the door and the milling machine), C and D

(single reflection on the wall), E diffracted component in the frame of the milling machine, and F (reflections from the machinery behind the RX).

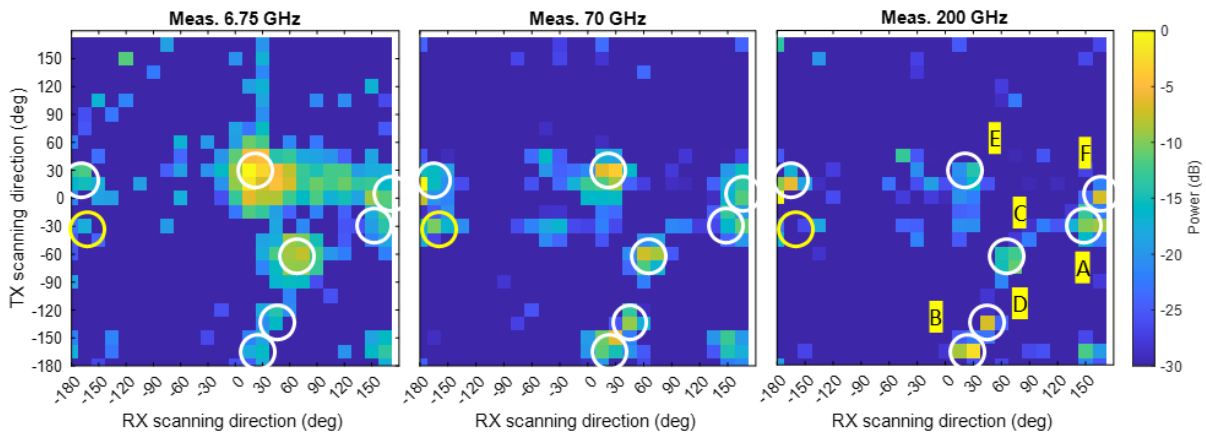


Figure 16: multi-band power azimuth/azimuth profile in the NLOS link TX1-RX4 in the machine room scenario.

The different scatterers are marked in the picture taken from the RX position.

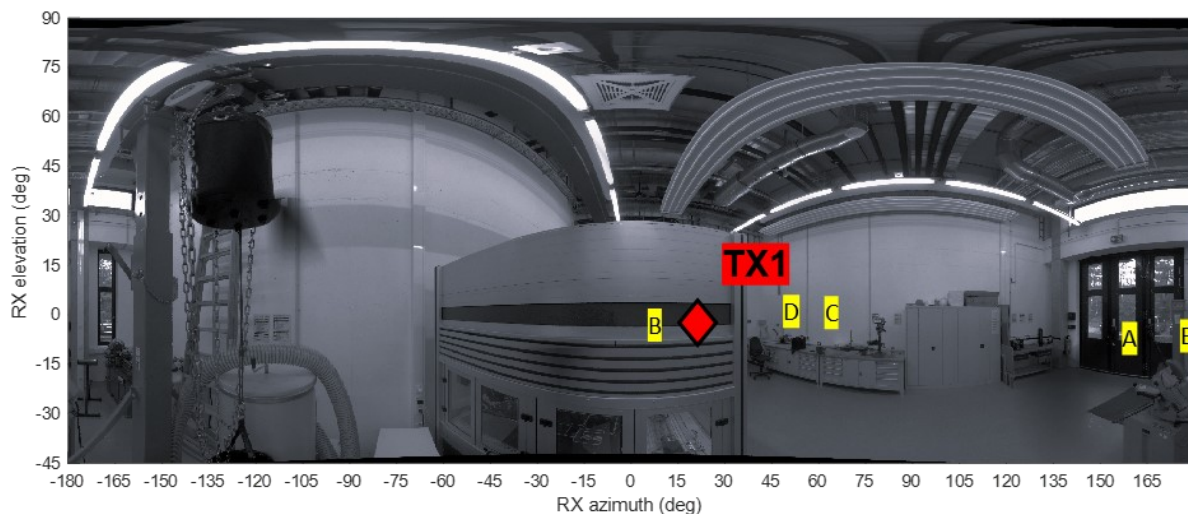


Figure 17: view from RX4 towards TX1 and the last interaction point of the identified MPCs in the NLOS link TX1-RX4.

5.3 Spatial/Temporal Properties of the Propagation Channel

The power azimuth/delay profile (PADP) at the RX in LOS for the different bands is shown in Figure 18. The propagation distance facilitates the identification of the origin of these MPCs. The wider pattern at sub-6 GHz is observed on the spreading of the LOS component in the angular domain.

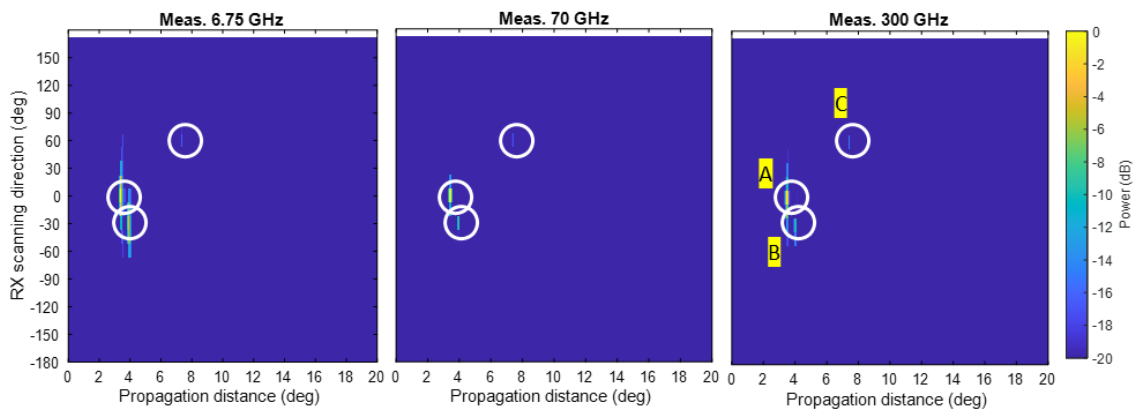


Figure 18: multi-band power azimuth/delay profile in the LOS link TX1-RX1 in the machine room scenario.

In the NLOS case, there is a strong direct diffracted on the edge of the milling head component (cluster E) visible at sub-6 GHz and at mmWave but not at THz. The other clusters identified and displayed in the power bi-azimuth profiles are shown with their propagation distance.

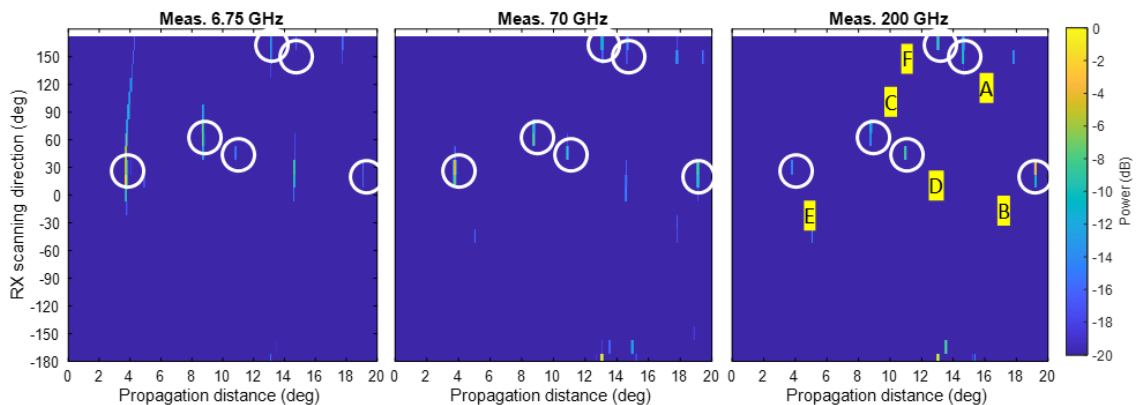


Figure 19: multi-band power azimuth/delay profile in the LOS link TX1-RX4 in the machine room scenario.

5.4 Temporal Properties of the Propagation Channel

The isotropic power delay profiles in the selected LOS and NLOS cases (normalized to the LOS component in both measurements) with the different scatterers are displayed in Figure 20.

In LOS, the three dominant paths (A, B, and C) are visible in the different bands. The gain of path B (reflection in the milling machine decays with frequency). Path C (reflection on the wall) has similar gains at sub-6 GHz and mmWave but is weaker at THz.

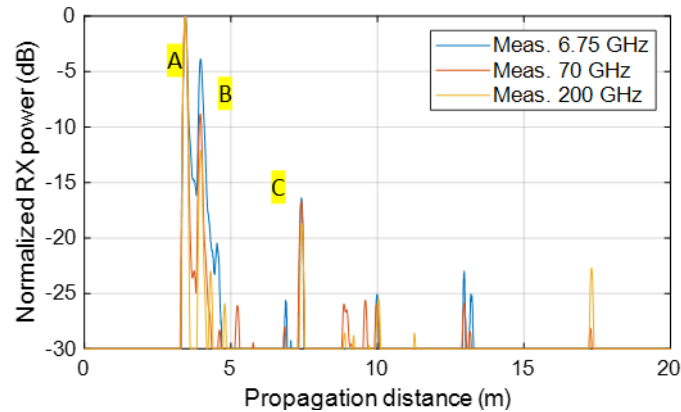


Figure 20: multi-band power delay profile in the LOS link TX1-RX1 in the machine room scenario.

On the other hand, in the NLOS measurement, the diffracted component in the milling machine (path E) is mostly visible at sub-6 GHz and mmWave, decreasing the gain with increasing frequency. The remaining dominant paths are present in the different bands.

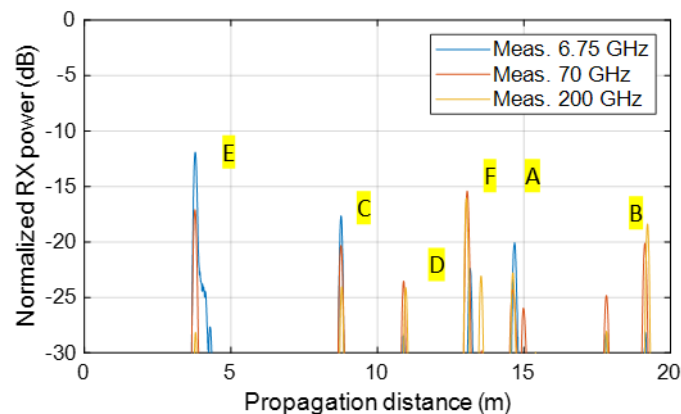


Figure 21: multi-band power delay profile in the NLOS link TX1-RX4 in the machine room scenario.

5.5 Polarimetric Properties of the Propagation Channel

The polarimetric decomposition of the power bi-azimuth profile in LOS is displayed in Figure 22. As expected, and predicted by Fresnel equations, since only the azimuth plane was scanned with an elevation of 0° , the polarimetric decomposition shows a higher reflection loss in the horizontal polarization in reflections on vertical planes. The reflection in the milling machine marked as cluster B is only visible in the polarization TX V and RX V. On the other hand, the reflection in the wall, marked as cluster C is visible in both polarization but with a higher gain also in the vertical channel.

A similar effect is also observed in the NLOS position displayed in Figure 23. Contrarily, the cluster E at 70 GHz and 200 GHz shows a higher gain in the horizontal than in the vertical

polarization. This path coincides in propagation distance and scanning angle of departure and arrival with a diffracted component on the edge of the milling machine.

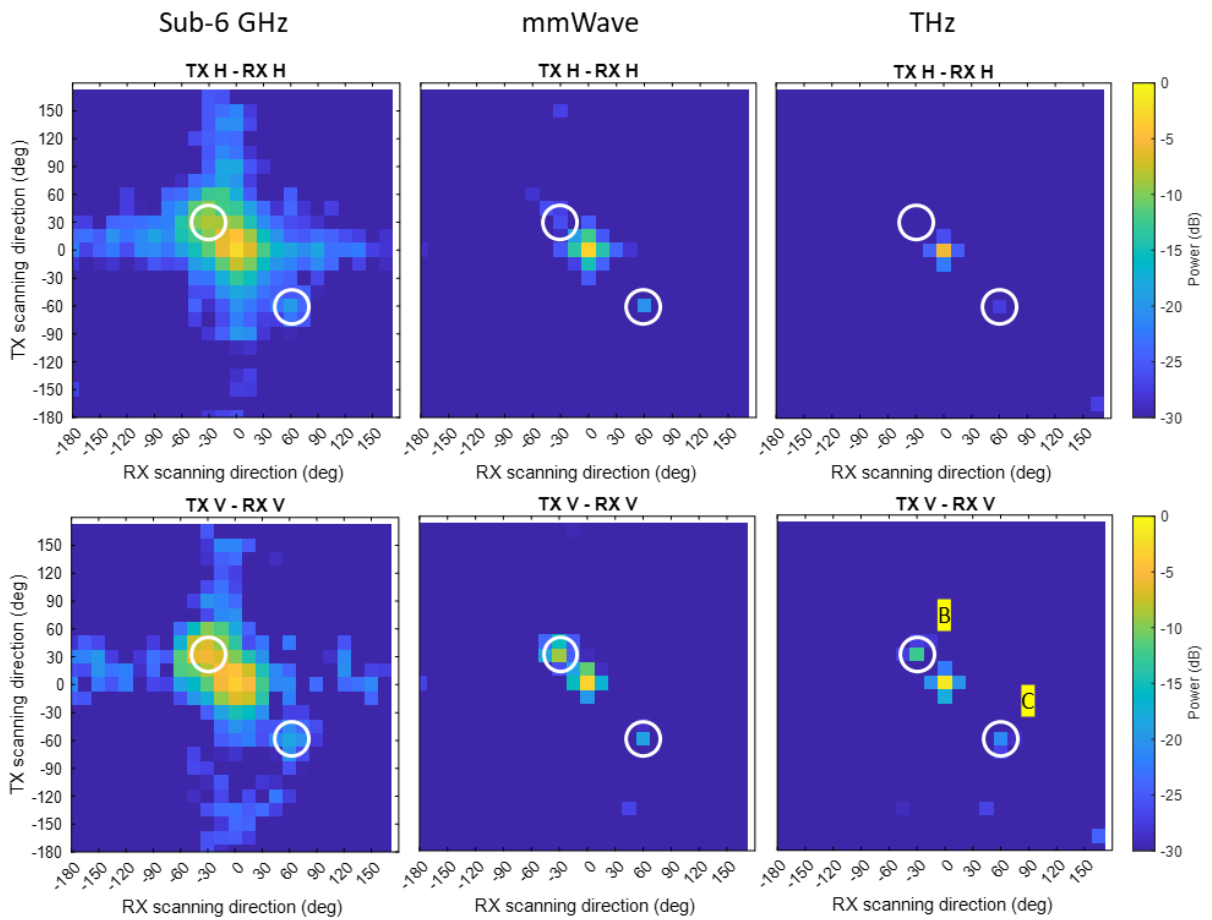


Figure 22: polarimetric multi-band power azimuth/azimuth profile in the LOS link TX1-RX1 in the machine room scenario.

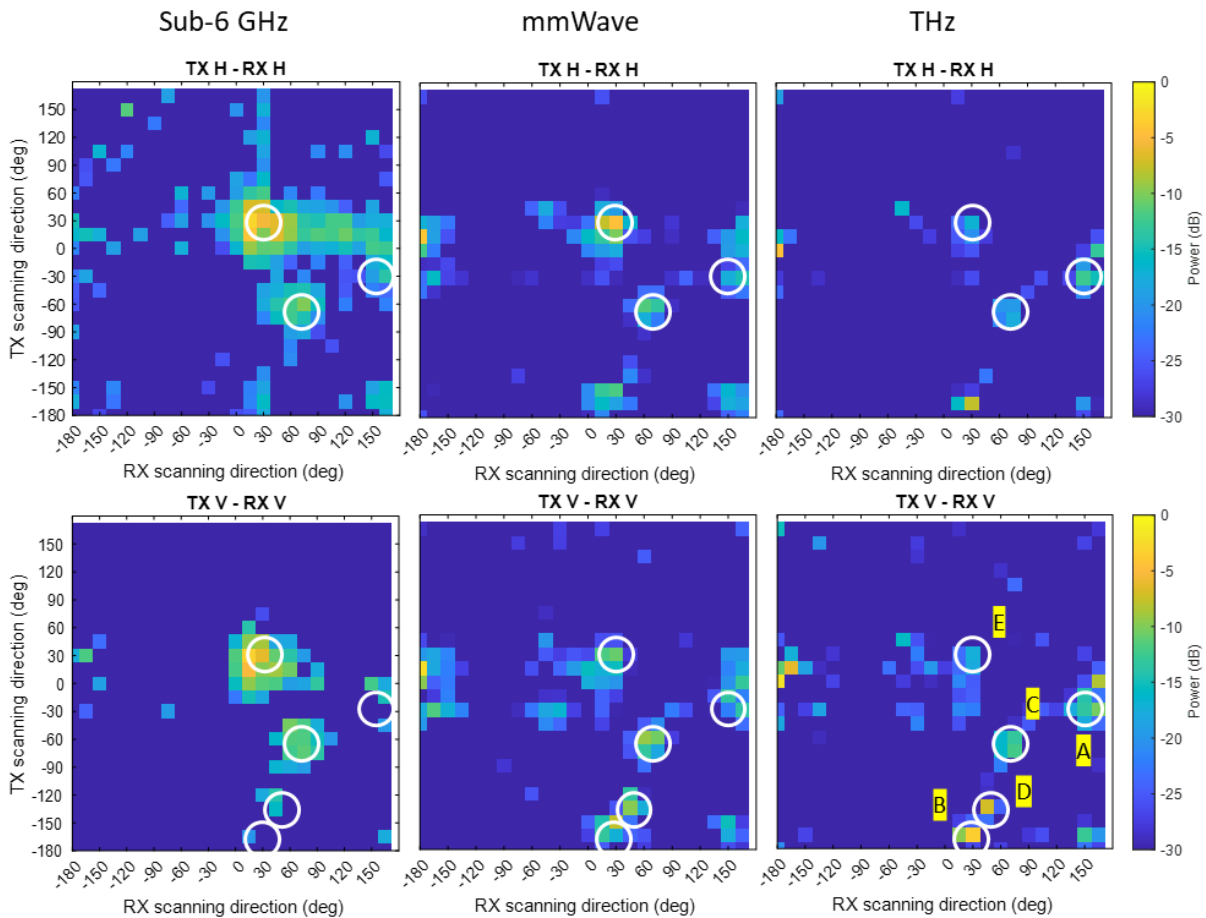


Figure 23: polarimetric multi-band power azimuth/azimuth profile in the NLOS link TX1-RX4 in the machine room scenario.

5.6 Analysis of Large-Scale Parameters

Due to the set-up and measurement capabilities, only the following LSPs were possible to calculate and analyze from the measurements: DS, ASA, and ASD.

The DS in the different links was calculated with the synthetic isotropic power delay profiles setting a dynamic range of 30 dB. The results are displayed in Figure 24. Similar values can be observed in the different bands in the LOS links (all excepting TX1-RX4, TX2-RX6 and TX2-RX7). A large difference on DS value is observed at sub-6 GHz in the NLOS link TX1-RX4. As seen from the PDP in figure, the strong diffracted component by the machine is much stronger at sub-6 GHz, which results in a larger DS.

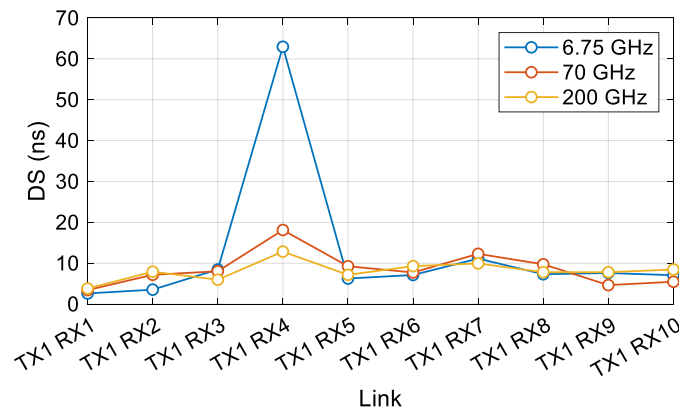


Figure 24: multi-band delay spread in the machine room scenario.

The azimuth spread of arrival in the different links is displayed in Figure 25. A high correlation on the trends can be observed between the different measured bands, which supports the idea of highly correlated channels over frequency.

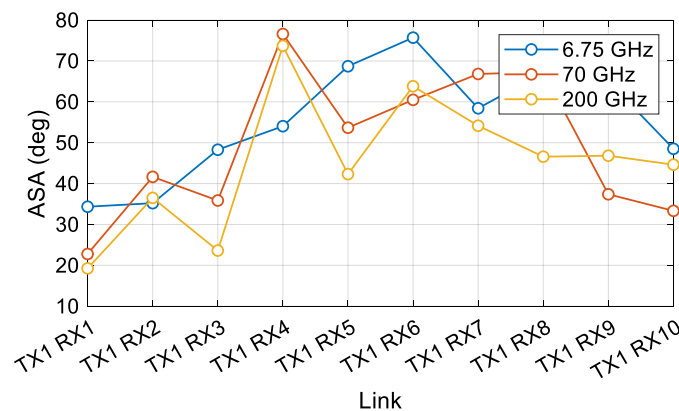


Figure 25: multi-band azimuth spread of arrival in the machine room scenario.

The angular spread of departure is displayed in Figure 26. Similar values are also observed in the different bands, however there is a large variation in the ASD in the LOS link TX1-RX2 at 200 GHz. The reason of this is the large difference on the path gain in a reflection at 180° azimuth of departure that is visibly stronger at 200 GHz than at lower frequencies, as analysed in detail in Figure 27.

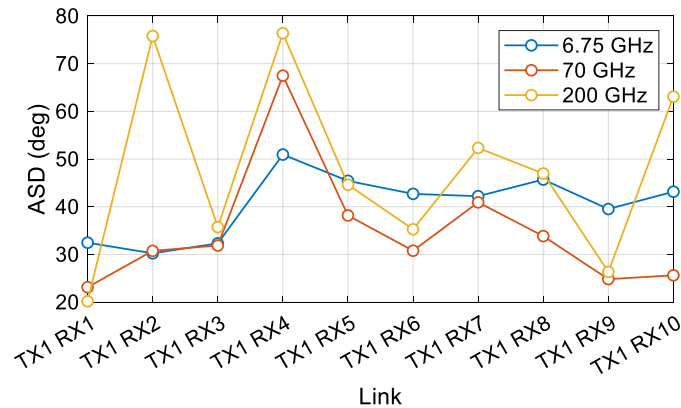


Figure 26: multi-band azimuth spread of departure in the machine room scenario.

This strong reflection that increases the power with frequency is most probably from the metallic frames of a rack located behind the Tx, depicted in Figure 27. The frames are approximately 4 cm width. This is small in electrical size compared to the wavelength at sub-6 GHz (the wavelength at the center frequency of 6.75 GHz is 4.4 cm), but it is large for the mmWave (wavelength is 0.43 cm) and sub-THz (wavelength at 200 GHz is 0.15 cm). Therefore, stronger reflections can be observed at higher frequencies.



(a)

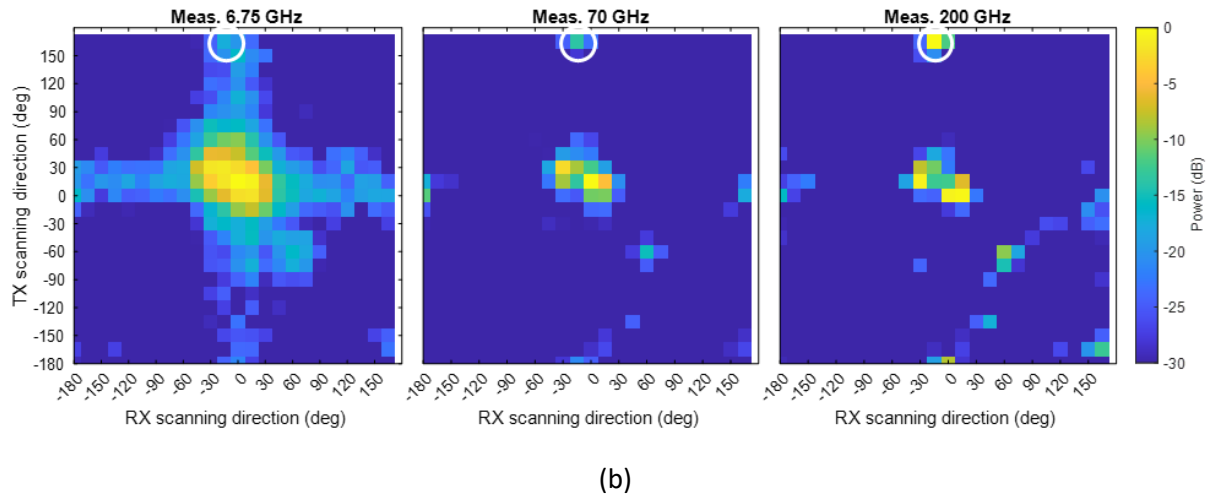


Figure 27: (a) metal rack and (b) multi-band power azimuth/azimuth profile in the LOS link TX1-RX2 in the machine room scenario.

The total RX power calculated with synthetic isotropic characteristics on the TX and RX and normalized to the shortest link (TX1-RX1) is displayed in Figure 28. A considerable drop on power can be observed between the LOS and NLOS positions, however, with similar trends in all the different bands.

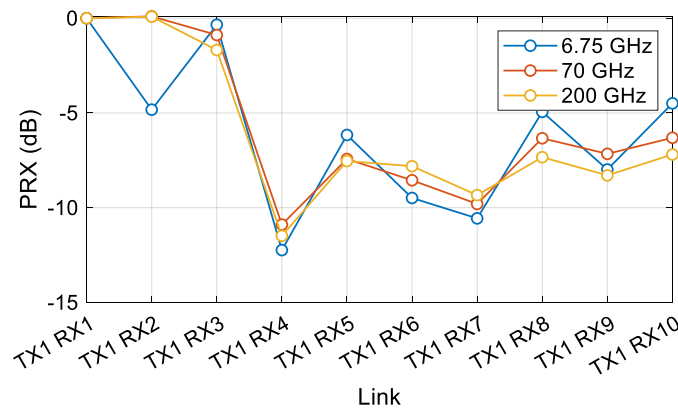


Figure 28: multi-band synthetic omni-directional received power in the machine room scenario.

The comparison of the measured path-loss with the free-space path-loss without distinction between LOS and NLOS is shown in Figure 29, showing a good agreement.

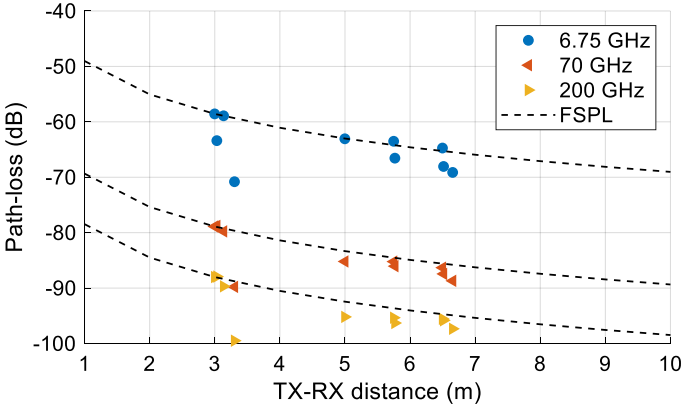


Figure 29: multi-band synthetic omni-directional path-loss in the machine room scenario.

The analysis of the LSPs showed a high correlation between the mmWave and sub-THz bands, even in NLOS. A lower correlation was observed with the sub-6 GHz, however, this could also be the result of the difference on antenna pattern between the measurements at sub-6 GHz and higher frequencies.

6 Summary and Concluding Remarks

6.1 Summary

This deliverable presents both the motivations and contributions for multi-band channel measurements and analyses. Firstly, the deliverable describes the measurement setup, which emulates a scenario of an antenna located at the top of a production unit connected to a 5G gateway supporting the complete production cell. The multi-band channel sounder simultaneously measures up to three different bands with a null-to-null measurement bandwidth of 6.75 GHz. The paper also presents the measurement results for nine different scenarios with different environments and two transceiver configurations in a practical indoor environment. Specifically, the sub-6 GHz, mmWave and optical band-based wireless communication channel measurements are performed in large industrial scenario (located in BOSCH factory in Blaichach, Germany). Moreover, the sub-6 GHz, mmWave and sub-THz band-based wireless communication channel measurements are conducted in machine laboratory (located in the Fraunhofer facilities in Ilmenau, Germany).

By analysing its synthetic omnidirectional power delay profiles (PDPs) of multi-band channel data measured from industrial scenarios, it can be seen that the main paths have similar gains in different frequency bands. Moreover, the measurements have shown that the dominant paths correspond to well defined specular reflections in the different elements of the environment (walls, metal frames, machines, etc.). These clusters and paths are present in the different frequency bands investigated during this set-up. There has not been observed a general dependence of the path gain with frequency, but from visual inspection, it seems to be that in the majority of the cases, the path gain decreases with increasing frequency. Furthermore, some paths have only been observed at lower frequencies and not at THz, and in other special cases, strong reflections in small objects (large electrical size compared to wavelength) have been observed at higher frequencies with a higher gain.

The channel is not as sparse as theoretically analysed due to the non-negligible influence of NLOS paths, especially in the mmWave band where a large amount of delay multipath components (DMC) power is observed. Moreover, for the optical band, the NLOS links also have a significant influence on channel and cannot be ignored directly, especially the industrial scenario with complex environments. Moreover, the multiple-input single-output (MISO) configuration can effectively improve the channel quality and uniformity of channel distribution. Furthermore, the difference in multipath increase as the reflector is closer to the Tx. Therefore, the location deployment of the Tx is crucial in practical OWC applications.

On the other hands, it can be seen from the analysis result of larger-scale parameter that mmWaves and sub-THz bands are highly correlated. Specifically, the presence of similar clusters in the different bands introduce a correlation on the propagation channel over frequency. Moreover, high order reflections were also observed in the sub-THz band. Mostly reflections on metallic surfaces as frames of machines, doors, or other machinery present in the environment. Furthermore, the stronger reflections can be observed at higher frequencies. The investigation on the polarimetric properties of the multipath components have shown a clear selective effect and that the path gain depends on the polarization of the transmitted signal (as predicted by Fresnel equations).

6.2 Concluding Remarks

The deliverable provides valuable insights into the measurement setups and results for RF-OWC channel characterization in industrial scenarios. The proposed hybrid RF-OWC system, channel model, and measurement results can help improve the performance of wireless communication systems in industrial settings. Specifically, it is worth emphasizing that non-line-of-sight (NLOS) paths have a non-negligible influence in practical channel environments, challenging the sparsity of the channel in complex environment. Therefore, the strategic deployment of the transceiver is crucial for improving channel sparsity and enhancing channel quality. Furthermore, the proposed channel estimation approach and the physical layer resource allocation and optimization strategies based on the channel sparsity should be redesigned and further studied to enhance the robustness of wireless communication networks in real industrial scenarios. On the other hand, considering that the channel attributes of different bands have their own characteristics, during the practical industrial wireless network deployment process, an appropriate band or hybrid band-based communication system should be carefully selected based on the channel characteristics and the complexity of the specific scenario to provide ultra-reliable and low-latency communication services.

References

- [ADT21] M. A. Arfaoui et al., "**Measurements-based channel models for indoor LiFi systems**," in *IEEE Transactions on Wireless Communications*, vol. 20, no. 2, pp. 827-842, Feb. 2021
- [AWZ18] A. Al-Kinani, C. -X. Wang, L. Zhou, and W. Zhang, "**Optical wireless communication channel measurements and models**," in *IEEE Communications Surveys & Tutorials*, vol. 20, no. 3, pp. 1939-1962, thirdquarter 2018
- [BSH18] P. Wilke Berenguer et al., "**Optical wireless MIMO experiments in an industrial environment**," in *IEEE Journal on Selected Areas in Communications*, vol. 36, no. 1, pp. 185-193, Jan. 2018.
- [DHE22] D. Dupleich et al., "**From Sub-6 GHz to mm-Wave: Simultaneous Multi-band Characterization of Propagation from Measurements in Industry Scenarios**," *2022 16th European Conference on Antennas and Propagation (EuCAP)*, Madrid, Spain, 2022, pp. 1-5
- [DML19] D. Dupleich et al., "**Multi-Band Propagation and Radio Channel Characterization in Street Canyon Scenarios for 5G and Beyond**," in *IEEE Access*, vol. 7, pp. 160385-160396, 2019
- [DML20] D. Dupleich, R. Müller, M. Landmann, J. Luo, G. Del Galdo and R. S. Thomä, "**Multi-band Characterization of Propagation in Industry Scenarios**," in *14th European Conference on Antennas and Propagation (EuCAP)*, Copenhagen, Denmark, 2020.
- [DMS19] D. Dupleich and e. al., "**Multi-band Indoor Propagation Characterization by Measurements from 6 to 60 GHz**," in *13th European Conference on Antennas and Propagation (EuCAP)*, Krakow, Poland, 2019.
- [HLZ22] M. Hofer, D. Löschenbrand, S. Zelenbaba, A. Dakić, B. Rainer and T. Zemen, "**Wireless 3GHz and 30 GHz Vehicle-to-Vehicle Measurements in an Urban Street Scenario**," *2022 IEEE 96th Vehicular Technology Conference (VTC2022-Fall)*, London, United Kingdom, 2022, pp. 1-5.
- [JSF23] W. Jiang and H. D. Schotten, "**Full-spectrum wireless communications for 6G and beyond: From microwave, millimeter-wave, terahertz to lightwave**," *2023 IEEE 3rd International Conference on Computer Communication and Artificial Intelligence (CCAI)*, Taiyuan, China
- [MMN18] A. A. Mamrashev, L. V. Maximov, N. A. Nikolaev and P. L. Chapovsky, "**Detection of nuclear spin isomers of water molecules by Terahertz time-domain spectroscopy**," in *IEEE Transactions on Terahertz Science and Technology*, vol. 8, no. 1, pp. 13-18, Jan. 2018,
- [RRE14] S. Rangan, T. S. Rappaport and E. Erkip, "**Millimeter-wave cellular wireless networks: Potentials and challenges**," *Proceedings of the IEEE*, vol. 102, no. 3, pp. 366-385, March 2014.
- [RXK19] T. S. Rappaport et al., "**Wireless communications and applications above 100 GHz: Opportunities and challenges for 6G and beyond**," in *IEEE Access*, vol. 7, pp. 78729-78757, 2019.

- [SSB19] O. Semiari, W. Saad, M. Bennis and M. Debbah, "**Integrated millimeter wave and sub-6 GHz wireless networks: A roadmap for joint mobile broadband and ultra-reliable low-latency communications**," IEEE Wireless Communications, vol. 26, no. 2, pp. 109-115, April 2019.
- [SSH18] E. Sisinni, A. Saifullah, S. Han, U. Jennehag, and M. Gidlund, "**Industrial Internet of Things: Challenges, opportunities, and directions**," in IEEE Transactions on Industrial Informatics, vol. 14, no. 11, pp. 4724-4734, Nov. 2018.
- [TSF21] H. Tataria, M. Shafi, A. F. Molisch, M. Dohler, H. Sjöland, and F. Tufvesson, "**6G wireless systems: Vision, requirements, challenges, insights, and opportunities**," in Proceedings of the IEEE, vol. 109, no. 7, pp. 1166-1199, July 2021
- [WWL19] Y. Wu, J. Wang, S. Lai, X. Zhu, and W. Gu, "**Transparent and flexible broadband absorber for the sub-6G band of 5G mobile communication**," Optical Materials Express, 8, 3351-3358, 2018.

[end of document]